2005:83

LICENTIATE THESIS

L

Hydrodynamic Lubrication of Rough Surfaces

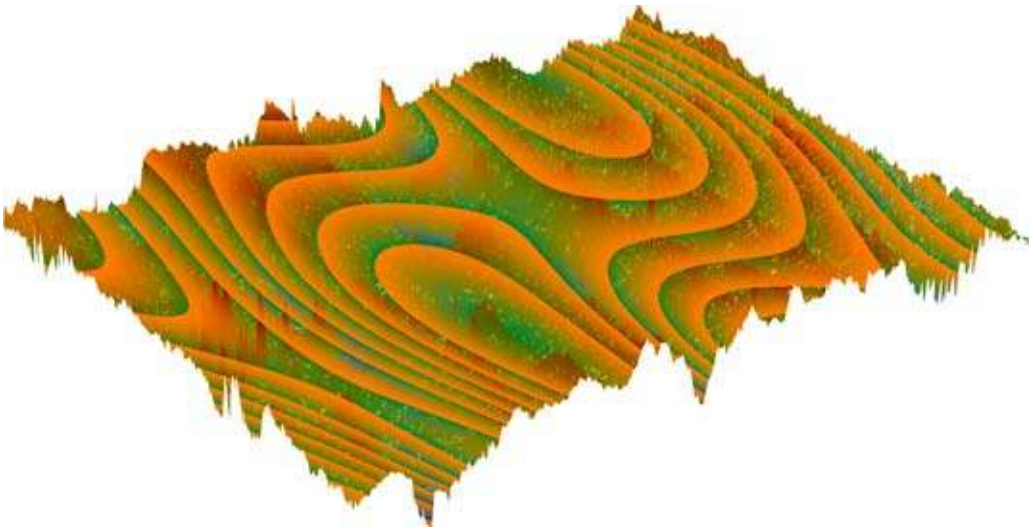

Fredrik Sahlin

Luleå University of Technology
Department of Applied Physics and Mechanical Engineering
Division of Machine Elements

2005:83 | ISSN: 1402-1757 | ISRN: LTU-LIC -- 05/83 -- SE

2005:83

LULEÅ
UNIVERSITY
OF TECHNOLOGY

HYDRODYNAMIC LUBRICATION OF ROUGH SURFACES

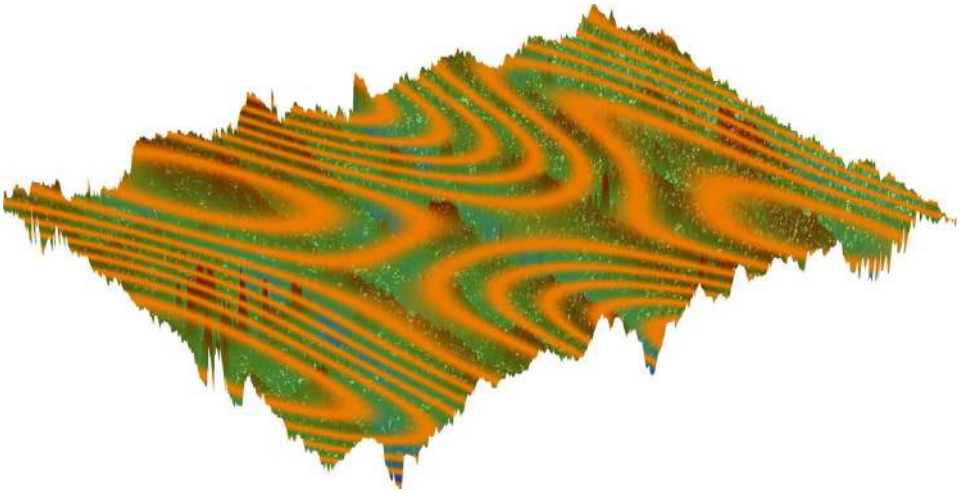

FREDRIK SAHLIN

Luleå University of Technology
Department of Applied Physics and Mechanical Engineering, Division of Machine Elements

2005 : 83 | ISSN : 1402 – 1757 | ISRN:LTU-LIC--05/83--*SE*

HYDRODYNAMIC LUBRICATION OF ROUGH SURFACES

Copyright © Fredrik Sahlin (2005). This document is freely available at

http://epubl.ltu.se/1402-1757/2005/83

or by contacting Fredrik Sahlin,

fredrik.sahlin@ltu.se

The document may be freely distributed in its original form including the current author's name. None of the content may be changed or excluded without permissions from the author.

ISSN: 1402-1757
ISRN: LTU-LIC--05/83--SE

This document was typeset in LaTeX 2ε

.

Abstract

Interacting surfaces are frequently found in mechanical systems and components. A lubricant is often added between the surfaces to separate them from mechanical contact in order to increase life and performance of the contacting surfaces. In this work various aspects of hydrodynamic lubrication are investigated theoretically. This is where interacting surfaces are completely separated by a fluid film which is often the desired operating condition of machine components when wear and friction is to be reduced. Different flow regimes can be identified within the scope of hydrodynamic lubrication.

If the surfaces are separated by a thick fluid film the influence from surface asperities is small and the surfaces can be treated as smooth. If the rate of change in film thickness with respect to the spatial directions is significantly large and if the flow velocity or Reynolds number is large, the ordinary fluid mechanical approach treating viscous flow with Computational Fluid Dynamics (CFD) has to be used. CFD is used to investigate influence from the use of an artificial microscopic surface pattern on one of the two interacting surfaces. The influence from the pattern is isolated from any other pressure generating effects by keeping the interacting surfaces parallel. Results are shown for different shapes of the micro-pattern. If the Reynolds number decreases, the system enters a regime called Stokes flow where the inertia effects are neglected. The full CFD approach is compared with the Stokes for various physical and geometrical cases.

If the change in film thickness is small in the spatial directions, the thin film approximation is applicable and the full momentum equations describing fluid flow together with the mass continuity equation can be reduced to the Reynolds equation. Depending on boundary conditions, low pressures can occur at location of expanding fluid gap leading to tensile stress applied to the lubricant. However, a real liquid lubricant can only resist small tensile stresses until it cavitates into a mixture of gas and liquid. This often happens close to atmospheric pressure due to contamination and dissolved air into the liquid and occurs at higher pressures than the actual vaporization. To avoid pressures reaching too low levels, a general cavitation algorithm applied to the Reynolds equation is presented that accommodates for an arbitrary density-pressure relation. It is now possible to model the compressibility of the lubricant in such a way that the density-pressure relation is realistic through out the contact. The algorithm preserves mass continuity which is of importance when inter-asperity cavitation of rough surfaces is considered.

For small film thicknesses the surface roughness becomes important in the performance of the lubricated contact. Even the smoothest of real surfaces is rough at a microscopic level and will influence the contact condition. The Reynolds equation still applies since the heights of the surface asperities are small compared to the spatial elongation. Treatment of the roughness of a real surface in a deterministic fashion is however beyond

the scope of today's computers. Therefore other approaches need to be employed in order to take the surface roughness into account. In this work a homogenization method is used where the governing equation of the flow condition is formulated with a two-scale expansion, the global geometry and the roughness. Solutions are achieved for the limit of the roughness wavelength, $\varepsilon \rightarrow 0$ and the method renders a possibility to treat the two scales separately. A method to generate dimensionless flow factors compensating for the surface roughness is developed. The flow factors, once solved for a particular surface, can be used to compensate for the surface roughness in any smooth global problem for any film thickness.

Acknowledgments

For the support and encouragement in the work included in this thesis I thank my supervisors, Associate Professor Sergei Glavatskih and Professor Roland Larsson at the Division of Machine Element. They provide great knowledge and experience in the field which has been of great value for the results presented here. I also send my gratitude to all the people at the Division of Machine Element for providing a stimulating research environment, and to the rest of the people at Luleå University of Technology who in various ways helped.

Special thanks goes to my former room mate Dr. Torbjörn Almqvist for his enthusiastic help in the first period of my Ph.D. studies. A second special thanks goes to my present room mate Tech. Lic. Andreas Almqvist for the invaluable scientific discussions and all collaborative research work. I am truly grateful for his inspiring ideas and his positivity. A third special thanks goes to Mr. Pär Marklund for all constructive discussions and collaboration in courses.

Finally I want to thank my family and friends who support me in ups and downs on the road.

Appended Papers

[A] F. Sahlin, S. B. Glavatskih, T. Almqvist, and R. Larsson. Two-dimensional cfd-analysis of micro-patterned surfaces in hydrodynamic lubrication. *Journal of Tribology*, 127(1):96–102, Jan 2005.

[B] F. Sahlin, A. Almqvist, R. Larsson, and S. B. Glavatskih. A cavitation algorithm for arbitrary lubricant compressibility. Submitted for publication in Tribology International, 2005.

[C] F. Sahlin, A. Almqvist, R. Larsson, and S. B. Glavatskih. Rough Surface Flow Factors in Full Film Lubrication based on a Homogenization Technique. Submitted for publication in Tribology International, 2005.

Additional Papers

[1] A. Almqvist, F. Sahlin, R. Larsson, and S. Glavatskih. On the dry elasto-plastic contact of nominally flat surfaces. In *Nordtrib 2004*, volume 11, pages 753–762, Tromso, Harstad, Hurtigruten, Norway, Jun 2004.

[2] A. Almqvist, F. Sahlin, and R. Larsson. An abbot curve based surface contact mechanics approach. In *World Tribology Congress III*, Washington, D.C., USA, Sep 2005.

Contents

Nomenclature

ϕ_x	Couette flow factor	
α	$r_{max}/\bar{h}$	
ϕ_s	Poiseuille flow factor	
$\bar{h}(x)$	Nominal fluid film clearance	m
$\bar{p}$	Dimensionless pressure, p/p_c	
$\bar{x}$	Dimensionless x-coordinate, $(6\eta u x)/(\beta(z_{max})^2)$	
β	Bulk modulus	Pa
χ	Solution to the local problem	
Δx	Local grid size	m
η	Dynamic viscosity	$\mathrm{Ns/m^2}$
Λ	$6\eta u/\beta$	
$\mathcal{L}_x$, $\mathcal{L}_y$	Typical length scales in x-, y-direction	m
$\mathbf{u}(x,y,z)$	Velocity field	m/s
ψ	Solution to the local problem	
ρ	Mass density	$\mathrm{kg/m^3}$
ρ_c	Density at atmospheric pressure	$\mathrm{kg/m^3}$
σ	Standard deviation	
θ	Dimensionless density, ρ/ρ_c	
r	Spatial coordinate or surface topography height	m
r_{max}	Maximum surface asperity height	m
ε	Wavelength measure of a local surface roughness scale	
ξ	x/ε	

A_{wall}	Wall area, $L_x \times L_z$	m^2
d	Groove depth	m
d^+	d/L_y	
F_x	Tangential wall force	N
F_x^+	Dimensionless tangential wall force, $100 * F_x L_y^2/(A_{wall}\eta u L_x)$	
F_y, W	Load carrying capacity	N
F_y^+	Dimensionless normal wall force, $100 * F_y L_y^2/(A_{wall}\eta u L_x)$	
G	Dimensionless surface topography height, $-z/z_{max}$	
g	Switch function, 0 if $\theta \leq 1$ and 1 if $\theta > 1$	
H	Dimensionless film thickness, $h/\bar{h}$	
$h(x)$	Film thickness,	m
h_0	Minimal fluid film clearance	m
K	Kurtosis of surface topography	
L_x, L_y, L_z	Fluid domain length in x-, y- and z-direction	m
N	Number of grid nodes for the cell problem	
p	Pressure	Pa
p^+	Dimensionless pressure, $100 * pL_y^2/(\eta u L_x)$	
p_c	Atmospheric pressure	Pa
Pe	Peclet number, $\rho u \Delta x/\eta$	
R_a	Average surface roughness	μm
R_q	RMS surface roughness	μm
Re	Reynolds number, $\rho u L_y/\eta$	
SK	Skewness of surface topography	
u, v, w	Velocity in x-, $y-$ and z-direction	m/s
$u_i(x,y,z)$	Velocity field tensor	m/s
w	Groove width	m
w^+	w/L_x	
x, y, z	Spatial coordinate directions	m
x^+	Dimensionless x-coordinate, $2x/L_x - 1$	
xd	Groove displacement	m
xd^+	xd/w	

Chapter 1

Introduction

The widespread range of mechanical applications with interacting surfaces and an increased industrial competition for improved performance and more cost effective products have lead to an increased attention to research in the science of friction, wear and lubrication, i.e. tribology. The rapid improvements of computers allow for more advanced tribological problems to be solved in a numerical fashion. This has led to an increased potential of numerical research and virtual experiments as a supplement to experimental approaches. Theoretical research is beneficial in terms of reducing expensive tribological testing and opens opportunities for more detailed investigations of the influence of specific physical parameters in order to increase the understanding of the physical problem considered.

In this thesis theoretical research is carried out to cover various aspects of sliding lubrication. A vast number of mechanical applications contain interfaces with sliding interacting surfaces. These interfaces operate under various loading conditions and relative sliding speeds. To reduce friction and minimize wear, the interacting surfaces are often separated by a thin layer of lubricant. Depending on the surface geometries, relative speed, surface topography and applied load among other things, the surfaces could be partly or completely separated from each other. Surfaces must form a converging gap or wedge to generate an effect of separation. When the lubricating fluid is dragged into the converging gap because of the relative motion of the surfaces, pressure will rise due to fluid compression because of the decrease in film thickness, producing a hydrodynamic load carrying capacity of the lubricated contact.

There are several lubrication regimes describing different operating conditions of the contact. An instructive illustration is shown in Fig. 1.1. The surface mean separation $\bar{h}$ scaled with the standard deviation of the surface roughness σ is plotted as a function of the lubricant viscosity and relative velocity divided by the applied load on the surfaces. For highly loaded lubricated surfaces at a small relative sliding speed, the regime is called boundary lubrication. In this regime all of the load is carried by the asperities of the surfaces. If the speed increases or load decreases the film thickness increases and the regime becomes the mixed lubrication. At this regime the load is carried by both the lubricating fluid and asperity contact. Next to the mixed lubrication regime is the hydrodynamic lubrication (HL) which is considered in this thesis. Within this regime the surfaces are completely separated by the fluid film and load is carried by hydrodynamic action.

Contacts operating in the hydrodynamic regime are found in various machine elements.

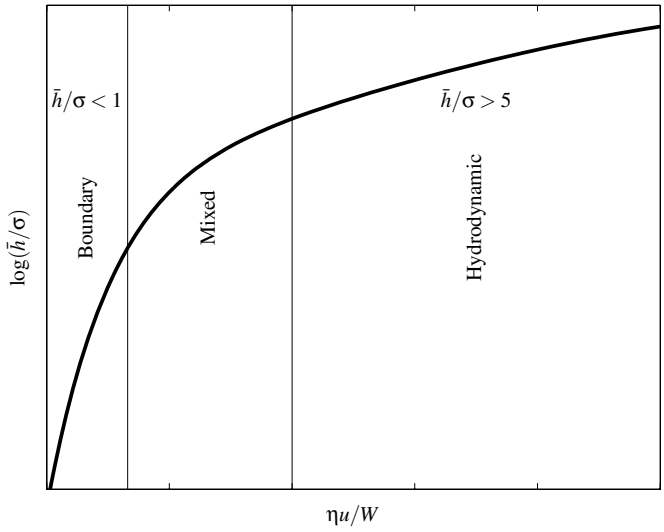

Figure 1.1: Different lubrication regimes.

Typical examples are the conformal hydrodynamic slider bearings, for example journal and thrust bearings. They are often designed to carry high loads and are typically found in engine crank shafts and turbines. Fig. 1.2 shows a thrust bearing having six pads with

Figure 1.2: A typical tilting pad thrust bearing.

self-adjusting tilt angle. The pads of the bearing are loaded against a collar on a rotating shaft. When the bearing is operating the pads are self-adjusted to form a converging gap. The lubricant is pulled into the interface to produce pressure and a load carrying capacity.

Bearing design is complex and involves optimizing several parameters such as the bearing geometry, lubricant properties and flow rate. The surface topography affects the performance of the bearing and is thus also an important design parameter. Simplistic design tools are available in the engineering community but their solutions are often limited in accuracy. More general comprehensive equations taking into account surface topogra-

phy are often difficult and time consuming to solve which limits their use in industry. For this reason theoretical research is important to gain more understanding of the effects of surface topography on a lubricated contact performance and to find more effective tools of bearing design.

Chapter 2

Hydrodynamic Lubrication

To theoretically describe the nature of a hydrodynamically lubricated contact the physics needs to be mathematically interpreted. The complexity of nature implies the need of a simplified interpretations. This is a process of deciding which physical parameters could be neglected and which must be retained in order to solve the problem in a way that is satisfactory. The simplifications of the problem also open an opportunity to isolate certain physical parameters and to study their specific effects on the system.

In the subject of hydrodynamic lubrication some important output parameters are friction force, pressure and load carrying capacity of the surfaces, film thickness, temperature and the flow field. Friction force and load carrying capacity are properties that can directly be related to the performance of the bearing. Most often a small coefficient of friction is desired in a bearing.

In this thesis, is the main focus is pressure and load carrying capacity. But friction force and velocity field are also considered. To treat these properties various fluid mechanical problems are considered by solving equations governing different regimes of fluid flow. The equations considered in this work are derived and discussed in Appendix 𝔸.

The physical scales in a hydrodynamic contact are of importance. Consider Fig. 2.1 which is a schematic view of a lubricated contact of two wavy surfaces. The lower surface is sliding with a velocity u dragging liquid lubricant (White) with viscosity η and density ρ into the contact. $\mathcal{L}_x$ and $\mathcal{L}_y$ are typical length scales for the global geometry irregularities. When modeling such a contact there are several important factors to consider. The values of η, ρ, u, h and the ratio $\mathcal{L}_y/\mathcal{L}_x$ play important roles. Also the surface topography visualized in the enlarged elliptic area is an important factor to consider. It should be noted that the scales of the surface topography are highly exaggerated. The local topography ratio of scales is typically of the order of $\mathcal{L}_y/\mathcal{L}_x \sim 10^{-2}$. All these properties determine which governing equations can be used to simulate the fluid mechanics. Let us categorize three types of equations valid in different sub regimes in hydrodynamic lubrication, namely:

1. Navier-Stokes equations
2. Stokes equations
3. Reynolds equation

All these sub regimes are affected by the surface topography if the film thickness h is small. These equations are derived and discussed in Appendix 𝔸. The Navier-Stokes equations

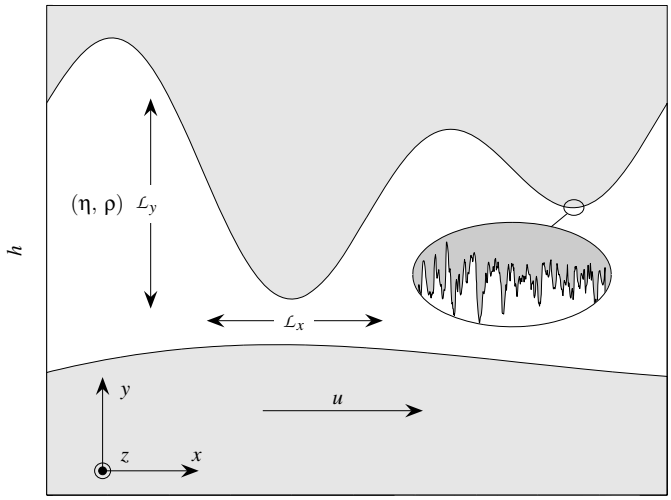

Figure 2.1: Different scales of a lubricated contact.

are the most general and are applicable to all hydrodynamic sub regimes. The Stokes equations which are simplifications of the Navier-Stokes are applicable to viscous flow with small Reynolds numbers. Reynolds equation is the most simplified and is considered in thin film flow with small Reynolds numbers. The Stokes equations are valid whenever the Reynolds equation is valid. An attempt to visualize which sub regimes are govern by these equations considering *pressure* as the output variable is shown in Fig. 2.2. It is a map with the mean film thickness scaled with the standard deviation of the surface asperities on the vertical axis and the Reynolds number *Re* times the length scale ratio of the surface irregularities on the horizontal axis. The gradient color visualizes that the influence of surface asperities increases as the ratio $\bar{h}/\sigma$ decreases. The three different flow equation regimes are divided by the dashed lines. It is important to keep in mind that the locations of the divider lines are not exact and only reflects the trends to some extent. The work in the appended papers A, B and C are categorized in terms of the hydrodynamic regime in the map, Fig. 2.2.

All sub regimes within the map signifies high viscosity flow since the film thickness $\bar{h}$ is small compared to other spatial coordinates. The Navier-Stokes flow regime, see Fig. 2.2, signifies large Reynolds numbers and also a rapid change in film thickness with respect to the spatial coordinates. Here inertia forces of the fluid are significant. If the Reynolds number and the geometrical irregularities $\mathcal{L}_y/\mathcal{L}_x$ are decreased, inertia forces become negligible and the regime is switched to the Stokes flow sub regime. By decreasing the film thickness the sub regime becomes the thin film flow govern by the Reynolds equation. If the viscous effects can negligible the Euler equations are valid, however, they are not applicable in the field of hydrodynamic lubrication.

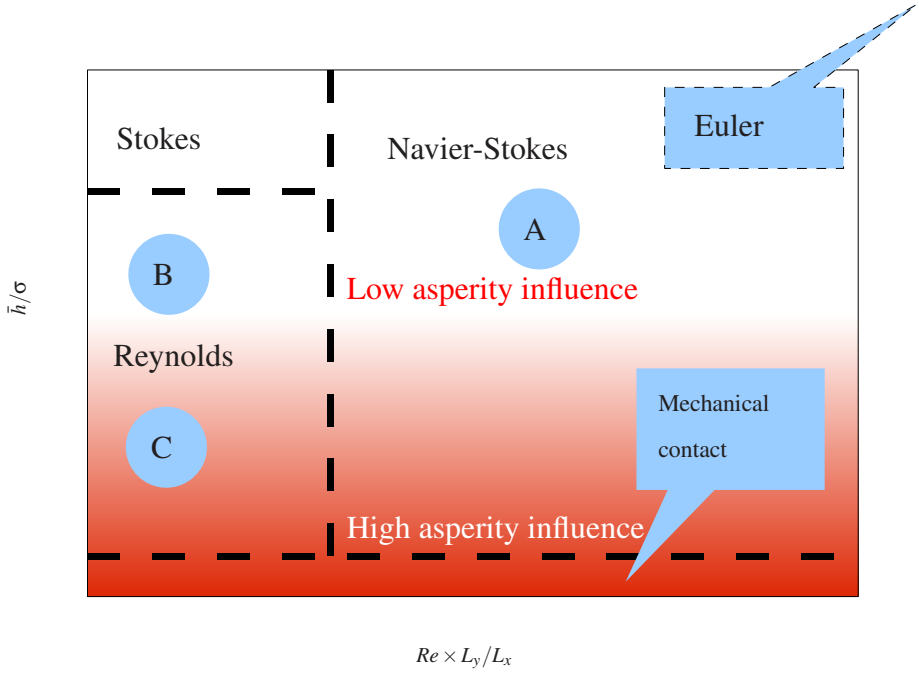

Figure 2.2: A qualitative map of hydrodynamic fluid sub regimes and the governing equations. The locations of the appended papers A, B and C in this map are also shown.

Chapter 3

Research Objectives

It is known that the surface roughness may affect lubricated contact performance in various ways. Even if the surfaces are smooth on a macroscopic level, asperities on a microscopic level may affect the overall performance in terms of pressure build-up, film thickness and friction. It is of importance to optimize surface topography to improve machine performance. This requires better fundamental understanding of contact conditions.

Deterministic computations of rough tribological contacts are difficult even with modern computers due to a large number of degrees of freedom imposed by the roughness. Thus, research aiming at finding simplified models that take into account surface roughness, thermal influence and asperity contact becomes important in order to develop effective computational tools for industrial applications.

The objectives of the present work are as follows:

1. To investigate how surface texture can improve sliding contact performance
2. To investigate the effect of surface topography on thin film contact performance
3. To develop engineering tools for design of efficient sliding contacts of rough surfaces

Chapter 4

Summary of Appended Papers

Paper A

In Paper A the effect of introducing an artificial surface texture or a micro-pattern to one of the interacting surfaces is investigated. The pattern is modeled as a pocket and the ratio of scales, $\mathcal{L}_y/\mathcal{L}_x$, of the pocket is in the order of 0.1 to 1 which is a large value when speaking of thin fluid film flows. Thus, the Navier-Stokes equations have to be used since the effects of fluid inertia are large. The influence from the pattern is isolated from any other pressure generating effects by keeping the interacting surfaces parallel. This approach provides a way to study of how surface texture affects the flow field and pressure for different Reynolds numbers and geometries of the pockets that constitutes the surface texture.

Paper B

It was shown in Paper A that pressure can be low in the diverging part of the pocket if the boundary pressure is low. A liquid lubricant cannot withstand tensile strain and will cavitate into a mixture of liquid and gas. This happens due to contamination particles and gas desolved in the liquid. For this reason the cavitation has to be taken into account when treating certain geometries and textures, typically if there is a considerable divergent part of the domain. It may also become important to consider the lubricant liquid as compressible. In Paper B a cavitation algorithm is developed where an arbitrary lubricant compressibility relation in the form $\rho = \rho(p)$ can be treated. This algorithm is developed for the thin film regime. In this work the influence from the surface asperities is neglected. This assumption is valid for values of $\bar{h}/\sigma$ that are sufficiently large, Fig. 2.2. However, with smaller surface separation the influence of surface asperities becomes important.

Paper C

In this paper an approach to deal with the influence of surface asperities is considered, Fig. 2.2. The thin film regime is considered and it should be noted that the local ratio of scales of the surface asperities is typically in the order of $\mathcal{L}_y/\mathcal{L}_x \sim 10^{-2}$ which allows the approach. Even if the surface is smooth on a macroscopic level the surface roughness on a microscopic level will often influence the performance of a bearing in terms of load

carrying capacity. Discreetly resolving the asperities and performing deterministic computations of the hydrodynamics demands computing powers beyond the scope of today's computers due to the numbers of degrees of freedoms involved. Here a homogenization technique is used where the global geometry is separated from the local roughness scale by a two-scale asymptotic expansion. The local scale is an arbitrary periodic function with a wavelength $\varepsilon \to 0$. With this approach a method of computing flow factors, compensating for the surface roughness, is developed. The flow factors can be computed for a measured surface topography with high resolution and once computed, they can be used as scale factors in a coarsely resolved global bearing problem.

Chapter 5

Conclusions

In this thesis, simulation of hydrodynamic lubrication has been considered. Different approaches in solving the fluid flow in the contact has been made.

1. The fluid mechanics of hydrodynamic lubrication between parallel surfaces is studied for isothermal, incompressible and steady 2D conditions. Normally no pressure rise in the film would occur when the surfaces are parallel. However, it is shown that the introduction of a micro groove on one of the surfaces affects the flow and pressure pattern. This gives a net pressure build-up and a load carrying capacity of the film. Negligible hydrodynamic effects are achieved when the advective terms are excluded from the Navier-Stokes equations, i.e when the Stokes equations are considered which proves the significance of inertia for this type of flow condition.

   It is shown that load carrying capacity increases with Reynolds number and the width of the groove. A general optimum is achieved when the depth of the groove is between 50 to 75 % of the filmthickness for all geometries and groove widths. The load carrying capacity can, to some extent, be related to the amount of circulation in the groove. A vortex appears at a certain value of groove depth. Near this value the maximum load carrying capacity is achieved.

2. When some part of the fluid gap is expanding pressure can become low and even cavitate into a mixture of liquid and gas. For some conditions it also becomes important to take the lubricant compressibility into account. To treat this, a generalized Reynolds equation accommodating for an arbitrary compressibility relation and cavitation was been derived. It has been shown that different compressibility models can produce significantly different results in a hydrodynamic pressure range. Load carrying capacity is especially sensitive to the type of compressibility relation used if the inlet is starved. Surface roughness close to the inlet has been shown to have important effects on load carrying capacity.

3. For small film thickness the surface roughness becomes important in most cases. Due to the amount of degrees of freedom required to resolve the surface roughness a homogenization technique for the compressible Reynolds equation was considered. With this technique a novel method of computing dimensionless flow factors compensating for the effects from arbitrary surface roughness has been developed.

By using the flow factors, the hydrodynamics can be solved on a coarsely resolved bearing geometry.

Chapter 6

Future Work

Computations of hydrodynamic problems involving surface roughness are complex due to the number of degrees of freedom involved in resolving the roughness. The future work is to continue studying various effects that surface roughness introduces in lubrication problems. The work will be extended to mixed lubrication regime. More physical quantities, such as thermal influence will be introduced in the theoretical analysis. Suggested future work will also cover developing engineering tools that can be used to predict different contact conditions and improve machine performance. These tools should be fast and able to cover most lubrication regimes.

Appendix 𝔸

Fluid Flow Equations

The fluid flow in hydrodynamic lubrication is govern by various equations depending on the physics to model. These are often described by non-linear partial differential equation and solving these equations describing the fluid motion is often complex. Therefore it is always desirable to simplify the modeling of fluid flow whenever possible. This is a process of determining scales of importance and dropping vanishing terms in the model which are not affecting the overall solution.

The basic governing equations for fluid motion of a viscous fluid are known as the Navier-Stokes equations of motion. They are derived by considering the dynamic equilibrium of forces acting at any given region of the fluid and involves conservation of mass and momentum.

𝔸.1 Forces

The forces considered are surface forces, body forces and inertia forces. Body forces are proportional to the mass of the fluid and are distributed throughout the mass, e.g. gravity force field. Here we will neglect the influence of body force. Surface forces are proportional to the extent of the area of the fluid and are exerted on an area element by the surroundings through direct contact. The surface forces can be expressed in terms of the stress tensor

$$\tau_{ij} = \frac{dF_{ij}}{dA} \tag{𝔸.1}$$

where F is the force tensor, A a control area and the first index denotes the components normal to the surface and the second components tangential to the surface. In three spatial dimensions the stress tensor has nine elements and completely specifies the stress at a point anywhere. The stress tensor is symmetric, i.e.,

$$\tau_{ij} = \tau_{ji} \tag{𝔸.2}$$

and thus has six independent components for three spatially dimensions. Also forces acting on line, so called line forces, can exist in nature and are typically surface tension but is not considered here. The inertia forces come from the acceleration of a fluid element, or

advection, and are expressed in terms of the material derivative

$$\frac{Du_i}{Dt} = \frac{\partial u_i}{\partial t} + u_j \frac{\partial u_i}{\partial x_j} \tag{𝔸.3}$$

The derivative describes the change in velocity as the element moves in space.

𝔸.2 Conservation of Momentum

By applying Newton's law of motion to an infinitesimal fluid element the equation of motion relating the inertia to the net force at a point for any continuum becomes

$$\rho \frac{Du_i}{Dt} = \frac{\partial \tau_{ij}}{\partial x_j}. \tag{𝔸.4}$$

which is the Cauchy's equation of motion. The constitutive equation for a particular fluid relates the shear stress to the strain rate. This relation is embedded in the stress tensor and could take a complex form. Many fluids may be approximated by a Newtonian model. The Newtonian model uses the assumption that the shear stress is linearly proportional to the strain rate. When the rate of shear strain is zero, the shear stress is zero.

𝔸.3 Navier-Stokes Equations

The Navier-Stokes equations are obtained by substituting a constitutive relation into Eq. (𝔸.4) and by assuming a Newtonian fluid becomes

$$\rho \frac{Du_i}{Dt} = -\frac{\partial p}{\partial x_i} + \frac{\partial}{\partial x_j}\left[2\eta e_{ij} - \frac{2}{3}\eta\left(\nabla \cdot \mathbf{u}\right)\delta_{ij}\right] \tag{𝔸.5}$$

which is a general form of the Navier-Stokes equations where η and ρ could be functions of for example pressure and temperature. δ is the Kronecker delta and the strain rate tensor $\mathbf{e}$ is defined as

$$e_{ij} \equiv \frac{1}{2}\left(\frac{\partial u_i}{\partial x_j} + \frac{\partial u_j}{\partial x_i}\right). \tag{𝔸.6}$$

If the Navier-Stokes equations are written in a three dimensional coordinate system they are three in numbers but include four unknowns, $\mathbf{u}$ and p. To be able to solve the problem, a complement to the conservation of momentum the principle of conservation of mass can be employed, called the continuity equation:

$$\frac{\partial \rho}{\partial t} + \frac{\partial}{\partial x_i}\left(\rho u_i\right) = 0. \tag{𝔸.7}$$

If the variation in viscosity is small the Navier-Stokes equations can be reduced to

$$\rho \frac{Du_i}{Dt} = -\frac{\partial p}{\partial x_i} + \eta\left[\nabla^2 u_i + \frac{1}{3}\frac{\partial}{\partial x_i}\left(\nabla \cdot \mathbf{u}\right)\right]. \tag{𝔸.8}$$

If the variation in density is small, $\nabla\mathbf{u} = 0$ and the Navier-Stokes and the continuity equations reduce to

$$\begin{aligned} \rho\frac{Du_i}{Dt} &= -\nabla p + \eta\nabla^2\mathbf{u} \\ \nabla\cdot\mathbf{u} &= 0. \end{aligned}$$

If the no variation in time occurs the Navier-Stokes equations can be further reduced:

$$\rho(\mathbf{u}\cdot\nabla)\mathbf{u} = -\nabla p + \eta\nabla^2\mathbf{u}. \tag{𝔸.9}$$

If the viscous effects (the rightmost term) are negligible the equations can be reduced to the Euler equations:

$$\rho(\mathbf{u}\cdot\nabla)\mathbf{u} = -\nabla p. \tag{𝔸.10}$$

𝔸.4 Stokes Equations

In lubrication problems however the fluid shear stress is normally high due to the small film thickness and cannot be neglected. On the other hand, since the shear stress often is high in hydrodynamic lubrication the fluid inertia or advection often becomes small in comparison. Hence, a more realistic simplification would be to neglect the advection:

$$-\nabla p + \eta\nabla^2\mathbf{u} = 0 \tag{𝔸.11}$$

which are known as the Stokes equations. These are more convenient equations to handle since the non-linear advective term is dropped. These equations are well suited for creeping flows with large viscosity and small velocities. In Paper A, Navier-Stokes Eq. (𝔸.9) and Stokes Eq. (𝔸.11) are compared in a hydrodynamic lubrication application.

𝔸.5 Reynolds Equation

The Navier-Stokes equations can be reduced further by assuming that the length scales $\mathcal{L}_y/\mathcal{L}_x \ll 1$ see Fig. 2.1. Consider the Stokes equations (𝔸.11) written in two dimensions:

$$\begin{aligned} -\frac{\partial p}{\partial x} + \eta\left(\frac{\partial^2 u}{\partial x^2} + \frac{\partial^2 v}{\partial x^2}\right) & \\ -\frac{\partial p}{\partial y} + \eta\left(\frac{\partial^2 u}{\partial y^2} + \frac{\partial^2 v}{\partial y^2}\right) &= 0. \end{aligned}$$

We will consider a scale analysis which could equally well be applied in three dimensions but for simplicity reason we consider a two-dimensional case here. Introduce the dimensionless parameters:

$$\bar{x} = \frac{x}{\mathcal{L}_x};\ \bar{y} = \frac{y}{\mathcal{L}_y};\ \bar{u} = \frac{u}{u_0};\ \bar{v} = \frac{v}{v_0};\ \bar{p} = \frac{\mathcal{L}_y^2 p}{\mathcal{L}_x \eta_0 u_0} \tag{𝔸.12}$$

Inserting these dimensionless parameters into Eq. (A.12), dividing by $(\eta_0 u_0)$ and multiplying by $\mathcal{L}_y^2$ gives:

$$\begin{aligned} -\frac{\partial \bar{p}}{\partial \bar{x}} + \left(\frac{\mathcal{L}_y}{\mathcal{L}_x}\right)^2 \bar{\eta}\left(\frac{\partial^2 \bar{u}}{\partial \bar{x}^2} + \frac{v_0}{u_0}\frac{\partial^2 \bar{v}}{\partial \bar{x}^2}\right) \\ -\frac{\mathcal{L}_x}{\mathcal{L}_y}\frac{\partial \bar{p}}{\partial \bar{y}} + \bar{\eta}\left(\frac{\partial^2 \bar{u}}{\partial \bar{y}^2} + \frac{v_0}{u_0}\frac{\partial^2 \bar{v}}{\partial \bar{y}^2}\right) &= 0. \end{aligned}$$

The ratio v_0/u_0 has the same order of magnitude as $\mathcal{L}_y/\mathcal{L}_x$. Neglecting these terms and assuming that that pressure variation in the y-direction can be neglected the equation becomes:

$$\frac{\partial \bar{p}}{\partial \bar{x}} = \bar{\eta}\frac{\partial^2 \bar{u}}{\partial \bar{y}^2} \tag{A.13}$$

and the Navier-Stokes equations have been reduced by applying the thin film approximation. This equation is in dimensionless form. However, let us express the equation with dimensional quantities and integration twice with respect to y yields

$$u = \frac{1}{2\eta}\frac{\partial p}{\partial x}y^2 + Ay + B. \tag{A.14}$$

A and B in this case are either constants or functions of x and can be solved by applying a boundary condition for u:

$$\begin{aligned} u = U_0 \quad at \quad y = 0 \quad and \\ u = U_h \quad at \quad y = h. \end{aligned} \tag{A.15}$$

where $h = h(x)$. Substituting (A.14) into (A.15) gives

$$B = U_0 \quad and \quad A = \frac{1}{h}(U_h - U_0) - \frac{h}{2\eta}\frac{\partial p}{\partial x}. \tag{A.16}$$

The Velocity becomes

$$u = \frac{1}{2\eta}\frac{\partial p}{\partial x}(y^2 - yh) + \frac{y}{h}(U_h - U_0) + U_0. \tag{A.17}$$

Revisiting the continuity equation for incompressible conditions:

$$\frac{\partial u}{\partial x} + \frac{\partial v}{\partial y} = 0 \tag{A.18}$$

and integration with respect to y from 0 to $h(x)$ yields:

$$-(V_0 - V_h) = x - \int_0^{h(x)} \frac{\partial u}{\partial x} dy \tag{A.19}$$

By substituting (A.17) into (A.19) interchanging the differentiation and integration through the use of applying Leibnitz's rule we get

$$\begin{aligned} -(V_0 - V_h) &= -\frac{\partial}{\partial x}\left[\frac{1}{2\eta}\frac{\partial p}{\partial x}\int_0^{h(x)}(y^2 - yh)dy\right] \\ &\quad -\frac{\partial}{\partial x}\int_0^{h(x)}\left[\frac{y}{h}(U_h - U_0) + U_0\right]dy - U_h\frac{\partial h}{\partial x} \\ -(V_0 - V_h) &= -\frac{\partial}{\partial x}\left(\frac{h^3}{12\eta}\frac{\partial p}{\partial x}\right) + \frac{\partial}{\partial x}\left[\frac{h(U_h + U_0)}{2}\right] - U_h\frac{\partial h}{\partial x} \end{aligned}$$

The left-hand term $-(V_0 - V_h) = \partial h/\partial t$. In this case $\partial h/\partial t = 0$ because of steady state conditions and the equation can be written:

$$\frac{\partial}{\partial x}\left(\frac{h^3}{12\eta}\frac{\partial p}{\partial x}\right) = \frac{h}{2}\frac{\partial}{\partial x}(U_h + U_0) + \frac{(U_0 - U_h)}{2}\frac{\partial h}{\partial x}. \tag{𝔸.20}$$

This is the incompressible Reynolds equation describing fluid film flows where the scales $\mathcal{L}_y/\mathcal{L}_x \ll 1$ and pressure variations across the film is neglected. The equation is here one dimensional with the y-component transformed to the film thickness equation h depending only on x. If the coordinate z was not dropped the film thickness would be a function of both x and z. In either case, all the Navier-stokes equations and the continuity equation are reduced to one equation with pressure as the dependent variable. If U_h zero and $u = U_0$ the Reynolds equation is reduced to

$$\frac{d}{dx}\left(\frac{h^3}{12\eta}\frac{dp}{dx}\right) = \frac{u}{2}\frac{dh}{dx}. \tag{𝔸.21}$$

In a similar form the compressible Reynolds equation can be written

$$\frac{d}{dx}\left(\frac{\rho h^3}{12\eta}\frac{dp}{dx}\right) = \frac{u}{2}\frac{d}{dx}(\rho h). \tag{𝔸.22}$$

This equation is used as a basis and modified in different ways in Paper B and C.

Paper A

Journal of Tribology 127 (2005) 96–102

Two-Dimensional CFD-Analysis of Micro-Patterned Surfaces in Hydrodynamic Lubrication

F. Sahlin, A. Almqvist, S. Glavatskih, R. Larsson

Luleå University of Technology, Division of Machine Elements, Luleå, SE-971 87 Sweden

(Received November 19, 2003; revised August 6, 2004)

Abstract

Results of a numerical study of the influence of micro-patterned surfaces in hydrodynamic lubrication of two parallel walls are reported. Two types of parametrized grooves with the same order of depth as the film thickness are used on one stationary wall. The other wall is smooth and is sliding with a specified tangential velocity. Isothermal incompressible two dimensional full film fluid flow mechanics is solved using a Computational Fluid Dynamics method. It is shown that, by introducing a micro-pattern on one of two parallel walls, a net pressure rise in the fluid domain is achieved. This produces a load carrying capacity on the walls which is mainly contributed by fluid inertia. The load carrying capacity increases with Reynolds number. The load carrying capacity is reported to increase with groove width and depth. However, at a certain depth a vortex appears in the groove and near this value the maximum load carrying capacity is achieved. It is shown that the friction force decreases with deeper and wider grooves. Among all geometries studied, optimum geometry shapes in terms of hydrodynamic performance are reported.

A.1 Introduction

The purpose of lubrication is to separate surfaces in relative motion in order to reduce friction and wear. The separation and load carrying capacity are achieved by generating a pressure in the fluid film between the surfaces. The most significant pressure build-up in hydrodynamic lubrication is achieved when a converging gap is allowed to form the surfaces. A relative velocity between the surfaces will start driving fluid into the gap leading to a pressure build-up.

In order to improve performance and efficiency and to reduce wear and the risk of failure in hydrodynamic lubrication, it is important to study various effects that can contribute to the pressure build-up.

The subject for this work is to investigate the influence of surface gesturing in hydrodynamic lubrication of two *parallel* surfaces. Experimental research in this area, such as reported in [1, 2] shows that significant improvements in hydrodynamic journal bearing performance can be achieved by surface gesturing. Textured reciprocating surfaces are studied experimentally in [3] where a clear reduction in friction force is found. Glavatskih, et al. [4] investigated hydrodynamic performance of thrust bearings and conclude that higher film thickness and lower power loss are obtained through the use of micro-patterned pads.

All mechanisms contributing to bearing efficiency using surface gesturing are far from known. Therefore theoretical analysis is important to be able to study individual effects. Numerical studies are presented in [5, 6] where Reynolds equation is used to simulate the effects of spherical grooves applied on a stationary surface in hydrodynamic lubrication.

One effect contributing to the load carrying capacity could be local cavitation at the diverging part of surface grooves. Local cavitation could contribute to the pressure build-up in a bearing. Such analysis is done by Brizmer et al. [7] who study parallel thrust bearings with spherical grooves using Reynolds equation with a cavitation model.

In the diverging part of the groove cavitation may occur leading to a two-phase flow. This two-phase flow will then enter the convergent part of the groove. To achieve a net pressure build-up this flow must be transformed to a single-phase liquid flow. Because of the groove and film geometry, this can only be achieved if an additional amount of liquid is supplied from outside the groove. In practical cases, it is unclear how this liquid supply to the dimples is achieved, especially when side leakage is considered. That is why there is a possibility that cavitation has a limited effect. Thus, other effects that may lead to a pressure build-up must be studied.

Arghir, et al. [8] report a Computational Fluid Dynamics (CFD) analysis of fluid flow between parallel surfaces with relative speeds. One of the surfaces contains a groove which is represented by three different geometries. The main conclusion of this study is that there is a net pressure build-up caused by the combined effect of the presence of a groove and of the increasing Reynolds number.

Although there are many physical effects contributing to hydrodynamic efficiency, it is important to study them individually to be able to distinguish between them. For different applications and running conditions, different physical effects will be present, contributing to the hydrodynamic performance in various ways. In this paper the fluid mechanical effects will be isolated and analyzed. The importance of inertia for certain types of flow conditions and micro-patterns will be discussed further in this work. The hydrodynamic performance in terms of friction force and load carrying capacity and how it depends on

groove geometry and flow conditions will be studied by using CFD.

A.2 CFD-Model

In this work the Navier-Stokes equations are solved using a commercial CFD code. The equations are applied without body force, with constant viscosity and density. The equations are steady and solved in the x- and y-direction only. With these properties the Navier-Stokes and the continuity equations can be written, respectively:

$$\begin{aligned} \rho(\mathbf{u}\cdot\nabla)\mathbf{u} &= -\nabla p + \eta\nabla^2\mathbf{u} \\ \nabla\cdot\mathbf{u} &= 0. \end{aligned}$$

The equations are solved in dimensional form, however, all results are represented in non-dimensional form in such way identical result are achieved for the same Reynolds number, *Re*. Hence, the dimensional values do not have any meaning, only the value of *Re*. Information about the non-dimensionalization of the quantities can be found in [9].

In this work, two types of geometries for the fluid domain have been studied. The first geometry is defined as the *cylindrical* geometry and is seen in Figure A.1. The groove is

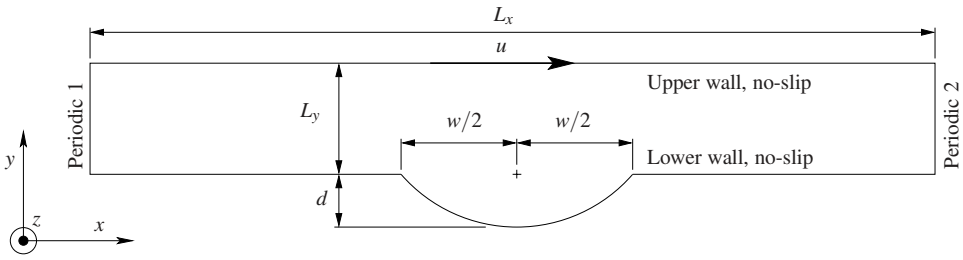

Figure A.1: The fluid domain of the cylindrical geometry. Included are the geometrical parameters and boundary conditions.

described by a circular arc of depth d and width w. The constant quantity $L_x = 1e-3$ m is the length in the x-direction of the domain and the constant quantity $L_y = 3e-5$ m is the film thickness of the fluid domain. In the same figure, the boundary conditions for the fluid domain are shown. The fluid is experiencing no-slip conditions at the walls. The upper wall is moving with a velocity u whilst the lower wall is stationary. The edges at high and low x-coordinates are bound by a periodic boundary. A symmetry condition is applied in the z-plane.

The second geometry is defined as the *splined* geometry and is seen in Figure A.2. The geometrical parameters for this case are defined as for the cylindrical geometry except that the groove is described as a splined curve. Another parameter, xd, is introduced to describe the x-displacement of the low y point of the groove. The same boundary conditions are applied for the splined as for the cylindrical geometry.

In all the equations, terms are discretized in space using second-order centered differencing apart from the advection. For these terms, a hybrid differencing scheme is used which is close to first-order accuracy [10]. This scheme is slightly better than upwind differencing because second-order central differencing will be used across streams and in regions of low flow where $Pe < 2$. If $Pe \geq 2$, upwind discretization will be applied. These

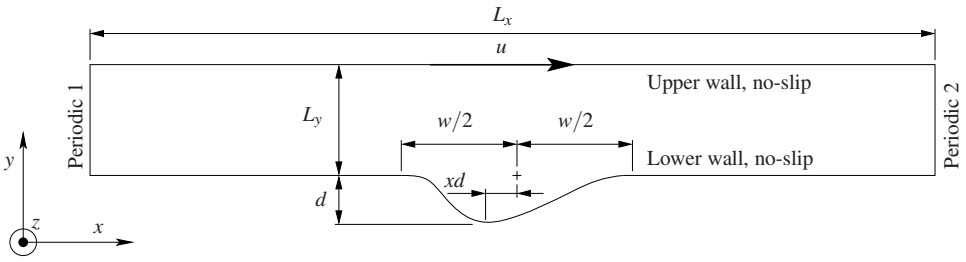

Figure A.2: The fluid domain of the the splined geometry. Included are the geometrical parameters and boundary conditions.

discretizations are based on a conservative finite-volume method [11]. For information of the computational grids and error analysis, see Sahlin [9].

A parametrized fluid model is used where certain parameters are being changed in a systematic order. All the parameters that are being varied, entirely independently from one another, are listed in Table A.1. Results from some complementary simulations with

Table A.1: Individually varied parameters.

$$w^+ \begin{Bmatrix} 0.15 \\ 0.20 \\ 0.25 \\ 0.30 \\ 0.35 \\ 0.40 \\ 0.45 \\ 0.50 \end{Bmatrix} \quad d^+ \begin{Bmatrix} 0.25 \\ 0.50 \\ 0.75 \\ 1.00 \\ 1.25 \end{Bmatrix} \quad xd^+ \begin{Bmatrix} -0.3 \\ 0 \\ +0.3 \end{Bmatrix} \quad Re \begin{Bmatrix} 40 \\ 80 \\ 120 \\ 160 \end{Bmatrix}$$

values different than those in the table will occasionally be shown.

A.3 Results and Discussion

Results are presented and discussed in terms of advection, fluid film pressure, streamlines and forces acting on the walls. It should be emphasized that the *fluid flow* effects are completely isolated from any other effects that might occur in a real thin film fluid flow. The interest in this paper is thus to analyze the fluid mechanical effects in hydrodynamic performance. However, other effects such as cavitation and thermodynamics would certainly influence the hydrodynamics.

A.3.1 Advective Influence

The advective (convective) contribution in the fluid flow can be studied by comparing the Navier-Stokes solution with the Stokes where the advective terms (inertia) are truncated from the Navier-Stokes equations. In Fig. A.3 the pressure distribution on the upper wall

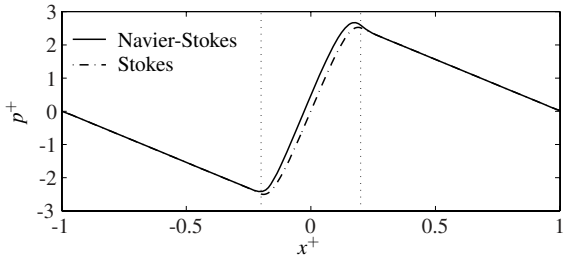

(a) $Re = 10$

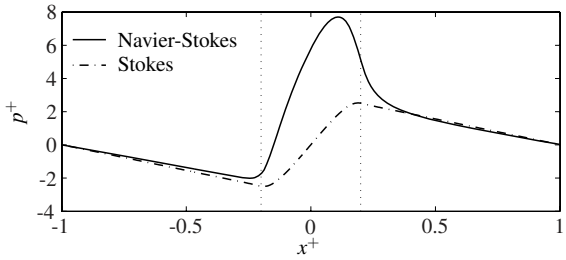

(b) $Re = 160$

Figure A.3: Comparison between Navier-Stokes and Stokes solutions for pressure distribution on the upper smooth wall for the cylindrical geometry. $w^+ = 0.2$ and $d^+ = 0.25$ for both plots. The vertical dotted lines represent the grove edges.

has been plotted as a function of the spatial dimension x^+ for Navier-Stokes and Stokes solutions respectively. In this figure the cylindrical geometry is used where *Re* is set to 10 in A.3(a) and 160 in A.3(b). With the value of *Re* in Fig. A.3(a), the Navier-Stokes and Stokes solutions are much alike. A small displacement to the left of the Navier-Stokes curve is seen next to the portion of the groove. When *Re* is increased in Fig. A.3(b), great differences between the two solutions arise. From Fig. A.3(b), the Stokes curve seems to be entirely antisymmetric whereas the Navier-Stokes curve shows a net pressure rise in the domain from the zero boundary.

Following the pressure curves in Fig. A.3(b) starting from low x^+, an almost linear pressure drop is encountered for both curves. Slightly before arriving at the groove edge, located at $x^+ = -0.2$, pressure increases rapidly for the Navier-Stokes solution producing a net pressure build-up in the fluid film. For the Stokes solution, the pressure continues its descent until it passes the groove edge where the curve changes to an almost linear pressure rise. The solutions from the Stokes case produces close to an antisymmetry-axis at the line $x^+ = 0$.

The area between the two curves in Fig. A.3(a) as well as in A.3(b) is equal to the contribution of inertia in the flow *only*, because the advective term is completely dropped in the Stokes equations. This confirms findings of a recent study made by Arghir et al. [8].

A quantitative measure of the difference between the Navier-Stokes and Stokes Solutions can be seen in Fig. A.4, which shows the dimensionless normal force F_y^+ as a function of w^+ for Navier-Stokes and Stokes solutions. As an example, the cylindrical geometry with the lowest simulated groove depth, $d^+ = 0.25$, is chosen. This is in order to provide as low an influence of inertia as possible. In Fig. A.4(a) $Re = 10$.

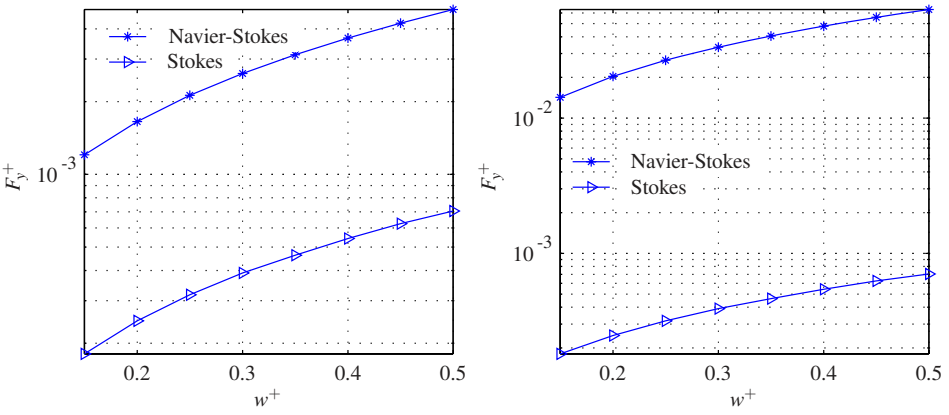

(a) $Re = 10$ (b) $Re = 160$

Figure A.4: F_y^+ on a 10-base logarithmic scale as a function of w^+ for Navier-Stokes and Stokes solution respectively, $d^+ = 0.25$.

It is seen that there is indeed a positive net force in the direction normal to the wall for the Stokes solution, evolving from diffusion.

However, the force for the Navier-Stokes solution is one order of magnitude greater. In Fig. A.4(b) the value of Re is 16 times greater and the force for the Navier-Stokes solution is two orders of magnitude greater than the force from the Stokes solution.

This shows the importance of the advective terms in the Navier-Stokes equations for this type of geometries and flow conditions. It implies that further simplifications to the Navier-Stokes equations would not be appropriate here.

A.3.2 Pressure Distribution

Figures of pressure distributions are shown with values at the periodic boundary set to zero only because it gives a convenient representation. The incompressible Navier-Stokes equations are solved, hence, the absolute pressure has no meaning in this study and the pressure distribution across the domain could be shifted any amount. Only the gradient of the pressure is affecting the flow and has meaning in this case.

Comparisons of pressure distribution for the cylindrical geometry are made in Fig. A.5 where p^+ is plotted as a function of the non-dimensional spatial dimension x^+ for different values of Re. $w^+ = 0.3$ is constant for all sub-figures but d^+ is varied between the sub-figures. All pressure distributions show a linear pressure drop at the beginning and at the end of the domain. The length in the x-direction where the pressure is deviating from this linearity at the mid part of the domain will be called *the affected elongation*. If Fig. A.5(a) where $d^+ = 0.25$ is considered, it is clear that the pressure build-up in the groove increases with the value of Re, and the differences are substantial. The pressure curves are convexly shaped across the entire affected elongation, i.e., the curvature $\partial^2 p/\partial x^2$ is negative throughout the pressure rise for all values of Re. With $Re = 160$, the maximum dimensionless pressure is about 9. In Fig. A.5(b) the groove depth is increased to $d^+ = 0.75$ and it is seen that the maximum non-dimensional pressure has increased to about 12. However, the curves do not show as extreme convexity as in the previous figure. In other words,

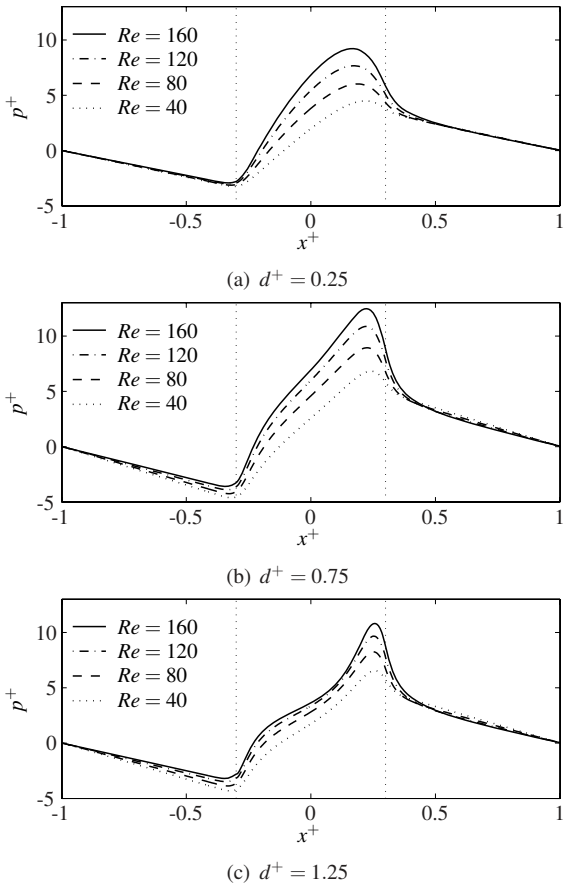

(a) $d^+ = 0.25$

(b) $d^+ = 0.75$

(c) $d^+ = 1.25$

Figure A.5: Upper wall pressure distribution for the cylindrical geometry with $w^+ = 0.30$. The vertical dotted lines represent the grove edges.

the curves are flattened out in the affected elongation. In Fig. A.5(c) the greatest groove depth $d^+ = 1.25$ is used. Here the pressure maximum is decreased compared to the case of $d^+ = 0.75$ and the difference in solutions between the Reynolds numbers are decreased. At the right half of the affected elongation the pressure distributions have concave shapes.

Some preliminary conclusions can now be made regarding how the pressure distributions are affected, which will later be proved with further results. By studying Fig. A.5 it seems that the affected elongation depends on the groove width w^+. On the other hand, the value of d^+ seems to affect the elevation and form of the pressure build-up curve. In terms of load carrying capacity, a convexity in the affected elongation which gives the maximum possible area beneath the curve is preferred. A flat pressure build-up with a higher maximum pressure will not lead to a higher load carrying capacity.

In Fig. A.6 the pressure distributions are plotted for the splined geometry with $w^+ = 0.5$ and $d^+ = 0.25$. Fig. A.6(a) is for a negative displacement of the low y-point with $xd^+ = -0.3$, Fig. A.6(b) for $xd^+ = 0$ and Fig. A.6(c) for a positive displacement with $xd^+ = +0.3$. As the affected elongation is nearly the same for all sub-figures, it can be confirmed

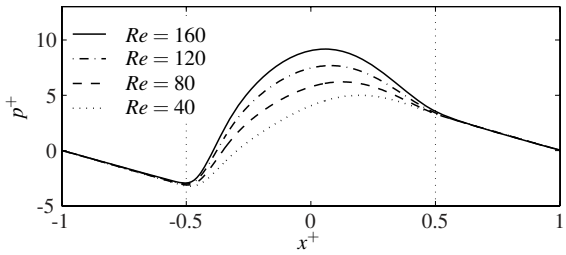

(a) $xd^+ = -0.3$

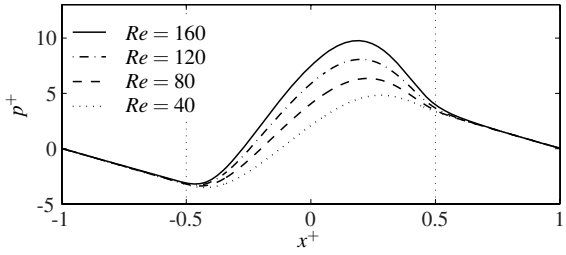

(b) $xd^+ = 0$

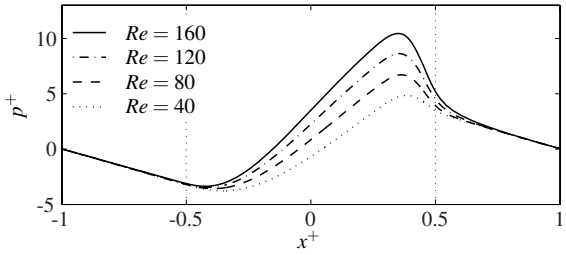

(c) $xd^+ = +0.3$

Figure A.6: Upper wall pressure distribution for the splined geometry used with $d^+ = 0.25$ and $w^+ = 0.50$. The vertical dotted lines represent the grove edges.

that it strongly depends on the value of w^+. It seems that the pressure distributions in Fig. A.6(a) provide highest load carrying capacity. When the groove is symmetric, in Fig. A.6(b), the rising-pressure zone flattens out slightly which may lead to lower load carrying capacity. In Fig. A.6(c) where $xd^+ = 0.3$, the rising-pressure zone flattens out further but a slightly increased pressure maximum is noted. If the assumptions about the load carrying capacities are true, the magnitude of the pressure maximum in the domain is not of primary importance in the sense of hydrodynamic performance. More important would be to achieve a shape of the pressure distribution which is as much convex at the affected elongation as possible.

A.3.3 Streamlines

Streamlines can give a qualitative idea about how the flow is ordered, if any vortexes or irregularities of the flow exist and, in that case, where they develop and what influences they have on the hydrodynamic performance. Streamlines are expressed in terms of the

scalar stream function ψ and along a streamline $\psi = constant$. The velocities can be found in terms of the derivatives of ψ as $u = \partial\psi/\partial y$ and $v = -\partial\psi/\partial x$.

In Fig. A.7, streamlines for the cylindrical geometry are plotted, all with $Re = 40$

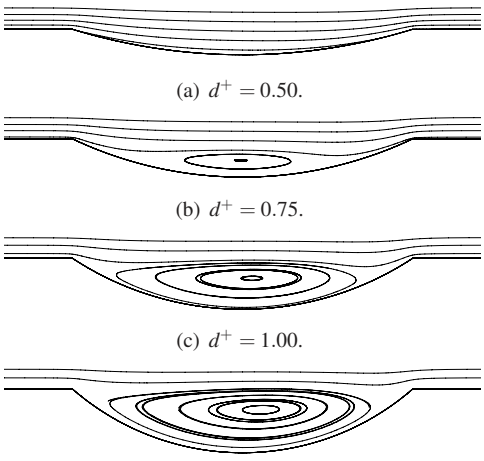

(a) $d^+ = 0.50$.

(b) $d^+ = 0.75$.

(c) $d^+ = 1.00$.

(d) $d^+ = 1.25$.

Figure A.7: Streamlines in the cylindrical geometry for different values of d^+ are plotted where $Re = 40$ and $w^+ = 0.20$.

and groove width $w^+ = 0.20$ but different groove depth d^+. In A.7(a) the streamlines are completely ordered and smooth, but as d^+ increases to a value between 0.5 and 0.75, a vortex is developed in the groove (see Sahlin [9] for a comparison with isobar plots for the same conditions). The vortex development can be related to a driven cavity flow phenomenon extensively studied by Shankar and Deshpande [12]. The size of the vortex is increased with increased d^+ and at $d^+ = 1.25$ the vortex is about the same size in the y-direction as the groove depth value. This shows that the vorticity is clearly dependent on groove depth.

Figure A.8 shows the effects of different values of Re. The cylindrical geometry is used with $w^+ = 0.15$ and $d^+ = 0.25$. As the value of Re increases, the size of the vortex increases. There is no vortex at a sufficiently low value of Re.

In Fig. A.9, streamlines are plotted for the cylindrical geometry with constant groove depth d^+ but different w^+. It can be seen that the vortex decreases in size with increasing groove width w^+ and constant Re. At a sufficiently large value of w^+ there is no vortex and no back-flow exists in the groove.

The vortex development obviously depends on the value of Re and how fast the geometry is changing, i.e. the value of dy/dx. These are properties which highly affect the advective influence whereby a connection is likely to exist between advection and the amount of vorticity. Let us therefore compare the full Navier-Stokes equations with the Stokes in terms of streamlines. Such a comparison is made in Fig. A.10. By comparing A.10(a) and A.10(b) it is obvious that the inclusion of advection leads to an earlier development of the vortex. However, when d^+ is doubled in A.10(c) and A.10(d), it can be seen that a vortex develops even without the advective influence and is entirely centered in the x-direction. With the advective influence the vortex center is moved to the right. Hence, the streamlines for the Stokes solution are completely symmetric in the line $x^+ = 0$. As

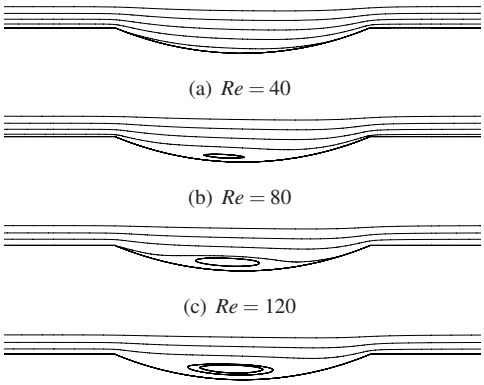

(a) $Re = 40$

(b) $Re = 80$

(c) $Re = 120$

(d) $Re = 160$

Figure A.8: Streamlines in the cylindrical geometry for different values of Re are plotted where $d^+ = 0.25$ and $w^+ = 0.15$.

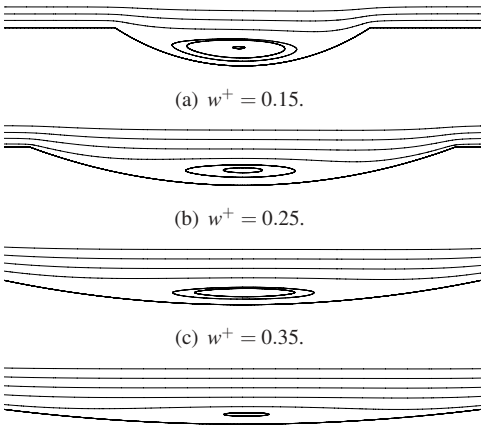

(a) $w^+ = 0.15$.

(b) $w^+ = 0.25$.

(c) $w^+ = 0.35$.

(d) $w^+ = 0.45$.

Figure A.9: Streamlines in cylindrical geometry for different values of w^+. $Re = 40$ and $d^+ = 0.75$ in all figures.

shown in the pressure plots, Fig. A.3, the pressure distributions for the Stokes solutions are close to antisymmetric at the same position.

A.3.4 Forces

Wall forces consist of both inertial and diffusive forces. These are attained directly from the CFD-solver.

It was shown in Fig. A.5 and A.6 that the pressure build-up was monotonically increased by increasing Reynolds number. This increase is further substantiated by Fig. A.11 where F_y^+ is plotted as a function of w^+. It is shown that the normal force also monotonically increases by increasing groove width w^+. A quantitative comparison between the

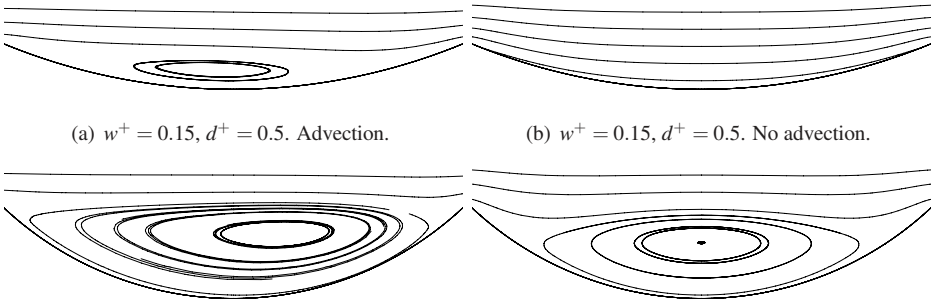

(a) $w^+ = 0.15$, $d^+ = 0.5$. Advection.

(b) $w^+ = 0.15$, $d^+ = 0.5$. No advection.

(c) $w^+ = 0.15$, $d^+ = 1$. Advection.

(d) $w^+ = 0.15$, $d^+ = 1$. No advection.

Figure A.10: Streamlines for Navier-Stokes solution left and Stokes solution right. The cylindrical geometry is used and $Re = 160$ for all.

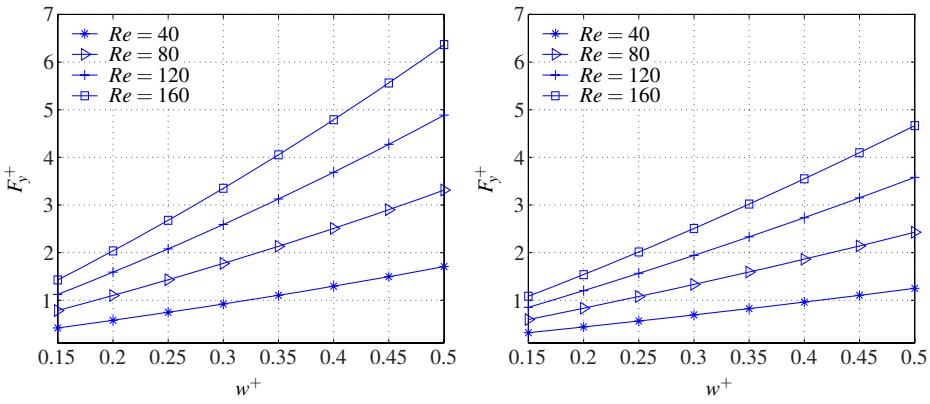

(a) Cylindrical, $d^+ = 0.25$

(b) Splined, $d^+ = 0.25$

Figure A.11: F_y^+ as a function of w^+ for various values of Re for the cylindrical geometry (top) and the splined with $xd^+ = 0$ (bottom).

cylindrical geometry and the splined geometry with a symmetrical groove displacement $xd = 0$ shows that higher normal forces are achieved with the cylindrical geometry for $d^+ = 0.25$.

Figure A.12(a) shows how the normal force is affected by different values of xd^+ for the splined geometry. As w^+ increases, the differences of F_y^+ between the three values of xd^+ also increase. It is clear that a negative value of xd^+ contributes positively to F_y^+, especially when w^+ is large. By comparing this curve with Fig. A.11(a) for $Re = 40$ it is noted that the splined geometry with $xd^+ = -0.3$ produces higher values of F_y^+ that the cylindrical. It should also be noted that F_y^+, for the special case of $xd^+ = 0.3$ in Fig. A.12(a), does not monotonically increase as w^+ increases. This is an exceptional behavior compared to all other geometries. If F_y^+ is instead plotted as a function of d^+, the differences are larger when d^+ is small and decrease when d^+ increases. This can be seen in Fig. A.12(b). It can also be seen that an optimum value of d^+ exists on each curve. There is a tendency that the optimum is displaced towards greater values of d^+ as xd^+ increases.

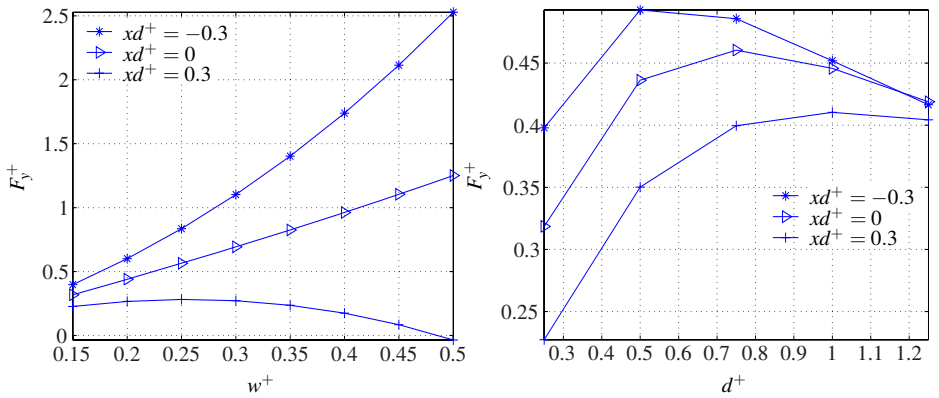

(a) $Re = 40$, $d^+ = 0.25$ (b) $Re = 40$, $w^+ = 0.15$

Figure A.12: F_y^+ for various values of xd^+ for the splined geometry..

In Fig. A.13 the non-dimensional friction force is plotted against d^+ for the cylindrical and splined geometry respectively. The cylindrical geometry produces lower friction

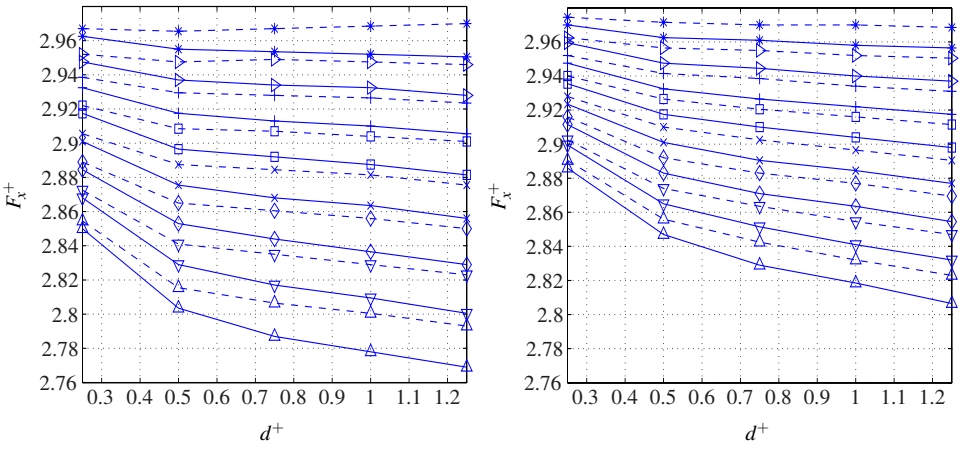

(a) Cylindrical (b) Splined, $xd^+ = 0$

Figure A.13: F_x^+ as a function of d^+ for the values of w^+ = $\{*0.15, \triangleright 0.2, +0.25, \square 0.3, x0.35, \Diamond 0.4, \triangledown 0.45, \triangle 0.5\}$. Solid line represents $Re = 40$ and dashed line $Re = 160$.

force than the splined geometry for all cases. This is partly explained by the fact that the cylindrical groove inherits a greater area than the splined, using the same width and depth, which in turn gives rise to a lower friction force. It is noticed that F_x^+ differs between Re and the difference is increasing as d^+ increases. The difference in F_x^+ between Re does not, however, change much by different values of w^+. F_x^+ decreases with increasing values of w^+ and d^+. However, F_x^+ shows a different behavior for the cylindrical geometry with high Re and low w^+. The smooth surface case, i.e. $d^+ = 0$, corresponds to a value of $F_x^+ = 3$ for a value of $Re = 40$. This shows that the textured surface will give rise to lower friction.

It was shown in Fig. A.11 that the cylindrical geometry produces greater normal force which is true for some cases. It was concluded in Fig. A.12 that the splined geometry is most effective, in terms of normal force, with a negative value of xd^+. Figure A.13 showed that the cylindrical geometry produces lower friction force compared to the splined geometry. The differences in friction force for different values of xd^+ is negligible. This concludes that, in most cases, the most beneficial geometries in terms of hydrodynamic lubrication are the cylindrical geometry and the splined geometry with $xd^+ = -0.3$. These two geometries are compared in Fig. A.14 and A.15, where the normal force is plotted as a function of d^+ for different values of w^+. At the lowest Reynolds number in Fig. A.14,

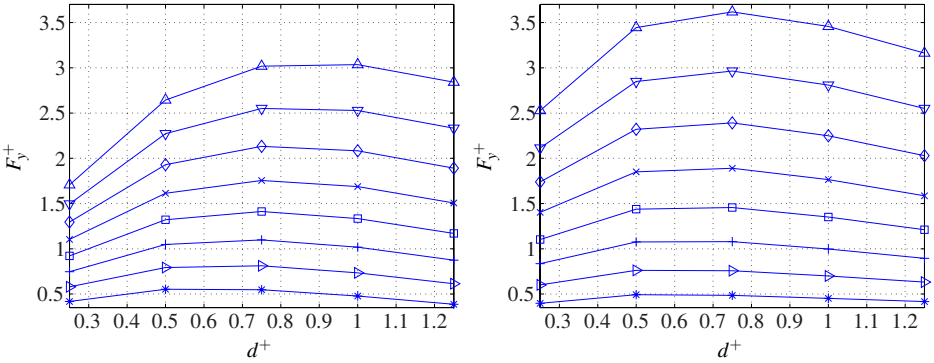

(a) Cylindrical, $Re = 40$ (b) Splined, $xd^+ = -0.3$, $Re = 40$

Figure A.14: F_y^+ as a function of d^+ for $Re = 40$ and the values of w^+ = $\{*0.15, \triangleright 0.2, +0.25, \square 0.3, x0.35, \Diamond 0.4, \triangledown 0.45, \triangle 0.5\}$. The cylindrical geometry (top) and the splined (bottom).

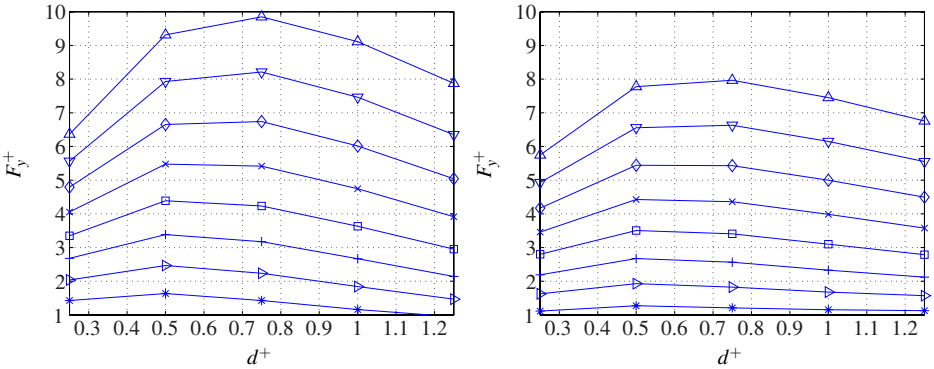

(a) Cylindrical, $Re = 160$ (b) Splined, $xd^+ = -0.3$, $Re = 160$

Figure A.15: F_y^+ as a function of d^+ for $Re = 160$ and the values of w^+ = $\{*0.15, \triangleright 0.2, +0.25, \square 0.3, x0.35, \Diamond 0.4, \triangledown 0.45, \triangle 0.5\}$. The cylindrical geometry (top) and the splined (bottom).

the splined geometry shows a higher load carrying capacity. At $Re = 160$ in Fig A.15 however, the properties are reversed and the cylindrical geometry shows higher normal forces. As stated earlier, there exists an optimal value of d^+ in terms of normal force,

which is also the case in this figure. At the lowest value of w^+ the maximum is located at $d^+ \approx 0.5$ in all cases represented. As w^+ increases, the maximum is displaced towards greater groove depths. This is also the case when *Re* is decreased. However, the optimum could in general be fit in the range $0.5 < d^+ < 0.75$ for most cases. No direct relation between the ratio d/w and forces can be found because of the strong individual effects of d^+ and w^+ respectively.

The conclusion that a certain maximum groove depth exists where an increase does not lead to further increase in load carrying capacity agrees with experiments made by Snegovskii and Bulyuk [1].

A comparison could be made between the second curve from the bottom representing $w^+ = 0.20$ in Fig. A.14(a) and the streamline plots in Fig. A.7(a) and Fig. A.7(b) which represent the same geometry and *Re*. It is seen that at $d^+ \approx 0.5$ where the maximum load carrying capacity is located, a vortex is beginning to form. When *Re* is increased, the vortex and the F_y^+-maximum appears at lower values of d^+ which is evident from Fig. A.8 and A.14 respectively. Making a comparison between Fig. A.9 and Fig. A.14 and A.15 reveals the relation between vortex formation and F_y^+-maximum in terms of different values of w^+.

This discussion shows that the normal force maximum appears close to the beginning of a vortex formation in the groove. This is true for most cases studied. Hence, the vortex affects the normal force in a destructive manner.

A.4 Conclusions

The fluid mechanics of hydrodynamic lubrication between parallel surfaces is studied for isothermal, incompressible and steady 2D conditions. The conclusions are summarized as follows:

1. An introduction of a micro groove on one of the surfaces affects the flow and pressure pattern. This gives a net pressure build-up and a load carrying capacity of the film. Negligible hydrodynamic effects are achieved when the advective terms are excluded from the Navier-Stokes equations.

2. Load carrying capacity increases with Reynolds number and groove width w^+. A general optimum is achieved when $0.5 < d^+ < 0.75$ for all geometries and groove widths. The load carrying capacity can, to some extent, be related to the amount of circulation in the groove. A vortex appears at a certain value of groove depth d^+. Near this value the maximum load carrying capacity is achieved.

3. The friction force decreases with increasing values of groove depth d^+ and width w^+.

4. The best hydrodynamic performance is achieved with the cylindrical geometry and the splined with a negative groove displacement xd^+.

Paper B

Submitted for publication in Tribology International (2005)

A Cavitation Algorithm for Arbitrary Lubricant Compressibility

F. Sahlin, A. Almqvist, R. Larsson, S. Glavatskih

Luleå University of Technology, Division of Machine Elements, Luleå, SE-971 87 Sweden

Received 12 October 2005

Abstract

A general cavitation algorithm is presented that accommodates for an arbitrary density-pressure relation. It is now possible to model the compressibility of the lubricant in such a way that the density-pressure relation is realistic through out the contact. The algorithm preserves mass continuity for cavitation caused by bearing geometry as well as surface topography. It is a commonly accepted physical assumption that the contribution of the pressure driven flow can be considered negligibly small in the cavitated region. This phenomenon is adopted in the present algorithm, which is similar to that of Elrod, and is modeled by a switch function that terminates the pressure gradient at the regions of cavitation. Results with this algorithm for different density-pressure relations are presented and discussed. Effects of inlet conditions, such as surface roughness and starvation, on load carrying capacity of the contact are analyzed.

B.1 Introduction

Cavitation usually occurs in the regions of diverging contact gap and implies sub-ambient pressures. These low pressures lead to a transformation of the liquid into a gas-liquid mixture. Different types of cavitation models have been proposed over the years to replicate this behavior in theoretical simulations. Some of the algorithms preserve lubricant mass continuity whilst others not. By simulating the behavior of rough surfaces, several cavitation regions might appear inside the contact and preserving mass continuity becomes crucial.

Jakobsson and Floberg [13] developed a mass preserving cavitation theory. They assumed that the pressure is constant in the cavitation region which means that the pressure gradient is zero. They derived a set of conditions to locate the cavitation boundaries. Later, Floberg extended their theory of cavitation and implemented it for a number of bearing types [14, 15, 16, 17]. Elrod [18] and Elrod and Adams [19] developed a cavitation algorithm where a single equation is used throughout the lubrication region without the need for explicit equations to locate the cavitation boundaries. They used a switch function to terminate the pressure gradient in the region of cavitation. Vijayaraghavan and Keith Jr [20] developed an algorithm in a similar way as Elrod and introduced more rigorous derivation which was further developed in [21]. This algorithm is derived under the assumption that the bulk modulus is constant. For real lubricants the bulk modulus varies with pressure. For a wide pressure range and under certain conditions it becomes important to use a realistic compressibility model for the lubricant. However, treating the bulk modulus as a constant could produce good results for a narrow pressure range.

The cavitation algorithm presented here uses Reynolds equation and is based on the assumption that the pressure gradient is zero in the cavitation region and that only Couette flow is present there. It inherits a similar switch function as the Elrod algorithm to modify Reynolds equation at the locations of cavitation. With this algorithm, an arbitrary density-pressure relation of the lubricant can be applied. Thus, measured compressibility factors from real lubricants can be used to achieve more realistic results.

B.2 Theory

The governing equation that constitutes the basis for the current algorithm is the Reynolds equation. A simple steady state form of this equation can be written as

$$\frac{u}{2}\frac{\partial(\rho h)}{\partial x} - \nabla\cdot\left(\frac{\rho h^3}{12\eta}\nabla p\right) = 0 \tag{B.1}$$

This is a mass continuity equation with the pressure p as the solution variable, describing Couette and Poiseuille flows, the first and second term respectively. It is non-linear but becomes linear if h, ρ and η are independent of p. The Reynolds equation is well suited for thin film flow, where h, and rate of change in h, is small with respect to the other spatial coordinates.

The density of all liquid lubricants depends on pressure among other variables. The density-pressure relation changes abruptly when the lubricant undergoes cavitation, resulting in a mixture of liquid and gas. At this condition the pressure remains close to constant whilst the density decreases rapidly. In order to mimic the behavior of cavitation, the Reynolds equation needs to be modified. It is convenient to use the density as the

dependent variable instead of pressure. We start by defining the non-dimensional density as

$$\theta = \frac{\rho}{\rho_c} \tag{B.2}$$

where ρ_c is the density at ambient pressure p_c. Since $p = p(\theta)$ it is possible to apply the chain rule on the pressure gradient, i.e.,

$$\nabla p = \frac{\mathrm{d}p}{\mathrm{d}\theta}\nabla\theta. \tag{B.3}$$

Combining Eqs. (B.1), (B.2) and (B.3) we get:

$$\frac{u}{2}\frac{\partial(\theta h)}{\partial x} - \nabla\cdot\left(\frac{\theta h^3}{12\eta}\frac{\mathrm{d}p}{\mathrm{d}\theta}\nabla\theta\right) = 0 \tag{B.4}$$

where the non-dimensional density θ is now the dependent variable and the only pressure influence in the equation is through the pressure derivative $\mathrm{d}p/\mathrm{d}\theta$. In the cavitation region the pressure is assumed to be constant, $p = p_c$, [13]. Hence, the pressure gradient is zero:

$$\nabla p = 0, \tag{B.5}$$

and no Poiseuille flow contribution exists in this region. However, the mass will be preserved and transported only by means of Couette flow. By definition, $\theta = 1$ at the cavitation boundary, thus to accomplish the termination of the pressure gradient we utilize the unit step function

$$g = \begin{cases} 1, & \theta > 1; \quad \text{Full film region} \\ 0, & \theta \leq 1; \quad \text{Cavitation region.} \end{cases} \tag{B.6}$$

Applying the above step function to the expression for the pressure gradient in Eq. (B.3) yields the Reynolds equation in the form

$$\frac{u}{2}\frac{\partial(\theta h)}{\partial x} - \nabla\cdot\left(\frac{\theta h^3}{12\eta}g\frac{\mathrm{d}p}{\mathrm{d}\theta}\nabla\theta\right) = 0. \tag{B.7}$$

Here, a single equation which preserves lubricant mass describes the flow both in the full film and in the cavitation region respectively. This is a more general form of already existing cavitation algorithms based on the Reynolds equation in that an arbitrary density-pressure relation could be used. Thus, more realistic density-pressure relations that accurately reflect the behavior of real lubricants can easily be applied.

B.3 Compressibility

The compressibility of the lubricant can be treated in several ways. It can be expressed through the bulk modulus defined as

$$\beta = \theta\frac{\mathrm{d}p}{\mathrm{d}\theta}. \tag{B.8}$$

If β is considered constant, integration ones gives the the expression for pressure and density:

$$p = p_c + \beta\ln\theta \Longleftrightarrow \theta = e^{\left(\frac{p-p_c}{\beta}\right)} \tag{B.9}$$

This expression for constant bulk modulus is sometimes used to model the compressibility of lubricants. However, in real lubricants β varies with density and thus the expression is only valid in a limited pressure range. Another is the Dowson & Higginson expression [22]:

$$\theta = \frac{C_1 + C_2(p - p_c)}{C_1 + (p - p_c)} \tag{B.10}$$

where the coefficients $C_1 = 0.59 * 10^9$ and $C_2 = 1.34$ was fitted to measured compressibility data of a mineral oil. Since the Reynolds equation on the form presented here can obey an arbitrary compressibility relation for the lubricant, it would be reasonable to use some other measured data as well as an input. Hence, as a test case for the current cavitation algorithm, the compressibility for a mineral oil will be used where data is taken from Tuomas and Isaksson [23]. They carried out measurements in a high pressure chamber with pressures ranging from ambient up to about 3 GPa. The coefficients in the Dowson & Higginson expression where fitted to the measured data. This fit can be seen in Fig. B.1 together with the measured data and the original Dowson & Higginson expression. The

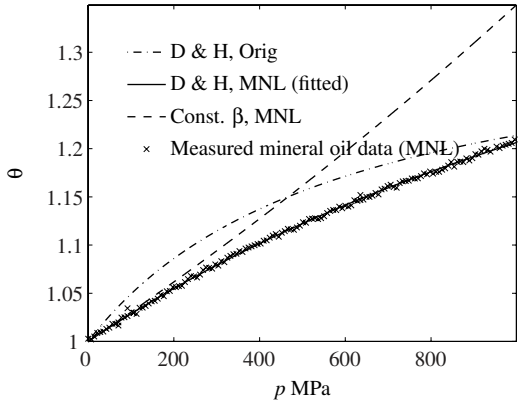

Figure B.1: Compressibility models for the measured mineral oil data. The original Dowson & Higginson expression with $C_1 = 0.59e9$ and $C_2 = 1.34$, a Dowson & Higginson expression fitted to the measured data with $C_1 = 2.22e9$ and $C_2 = 1.66$, an exponential expression with $\beta = 3.3$ GPa fitted at $\theta = 1$ for the fitted D & H expression.

relation in Eq. (B.9) is also plotted, where $\beta = 3.3$ GPa which is the bulk modulus taken for the curve fit at $\theta = 1$. The best correlation between the expressions can be observed in the proximity of ambient pressure but deviates exponentially with pressure rise. The same notation for the compressibility relations in Fig. B.1 will be used in the figures ahead. The acronym MNL is used as a label to show that the compressibility relation origins from the measured mineral oil data. The cavitation pressure $p_c = 10^5$ Pa will be used in the numerical examples. Cavitation and ambient pressure will be treated synonymously.

B.4 Numerical Examples

The Reynolds equation is discretized by using a central differencing on the Poiseuille term and a second order backward differencing on the Couette term. Because of the non-linear

nature of the problem, a fixed point iteration process on the form $\theta_n = f(\theta_{n-1}, ...)$ for $n = 0, 1, ...$ is used to solve the discrete system. The switch function g is updated each iteration. The iterative convergence of the solution is always ensured to be a value below 10^{-8} and the grid is ensured to be fine enough to produce a grid independent solution.

In order to compare solutions for different compressibility models etc., the following integral residual of the current solution ψ to a solution $\psi^\star$ is defined as:

$$\mathcal{S}^\star_\psi = \left| \int_0^{L_x} \psi^\star \mathrm{d}x - \int_0^{L_x} \psi \mathrm{d}x \right| \Big/ \left| \int_0^{L_x} \psi^\star \mathrm{d}x \right|, \tag{B.11}$$

which is the residual in load carrying capacity if the solution is pressure. In the numerical examples, only one dimensional problems will be considered where L_x is the domain length. This means that the geometries are treated as infinitely wide with no side leakage.

Dirichlet boundary conditions are used at the inlet (w) and the outlet (e) of the domain by specifying a constant pressure p or non-dimensional density θ. If $\theta < 1$ at the boundary, the domain will be termed starved, likewise if $\theta = 1$ the domain is flooded and if $\theta > 1$ the domain is pressurized. As a first comparative test case, a parabolic geometry modeled by

$$H = H_0 + A\frac{(x - L_x/2)^2}{(L_x/2)^2} \tag{B.12}$$

with the same physical dimensions and operating conditions as in Vijayaraghavan and Keith Jr [20], the geometry is seen in Fig. B.2. In Fig. B.3, a pressurized inlet is used

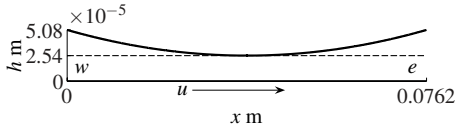

Figure B.2: A single parabolic slider geometry with $H_0 = 25\ \mu$m and $A = H_0$.

and the pressure solutions are shown from the Dowson & Higginson expression fitted to the measured mineral oil data and from the expression for constant $\beta = 6.9 * 10^7$ Pa, the same as applied in [20]. The solution from the constant β expression mimics the results

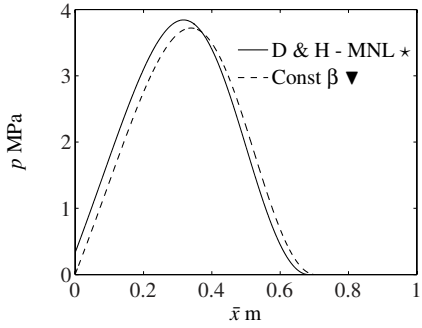

Figure B.3: Pressure solutions with boundary conditions $\theta_w = 1.0001$ and $\theta_e = 1$. $\beta\blacktriangledown = 0.069$ GPa with $\mathcal{S}^\star_p = 12$ %. $\eta = 0.039$ Pas and $u = 4.57$ m/s.

from [20] but differs from the Dowson & Higginson expression in load carrying capacity with 12 %. A large difference is expected since the Dowson & Higginson expression represents $\beta = 3.34$ GPa at $p = p_c$ which is significantly different from 0.069 GPa used in reference [20]. In Fig. B.4 the twin parabolic geometry used in [20] is shown and the corresponding pressure solutions are shown in Fig. B.5. The two pressure maxima are

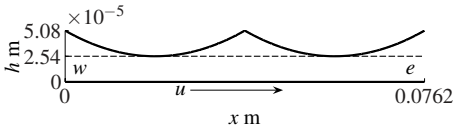

Figure B.4: A twin parabolic slider with $H_0 = 25\,\mu$m and $A = H_0$ m

similar but the pressurized inlet causes the pressure maximum to the left to be slightly higher (1.6 kPa). There is a difference in load carrying capacity of 15 % between the two compressibility relations. Continuing now with the same type of geometry as in Fig. B.2

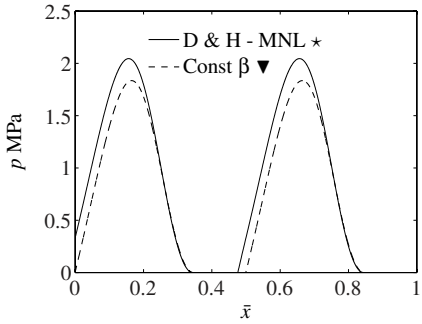

Figure B.5: Pressure solutions across the domain with boundary conditions $\theta_w = 1.0001$ and $\theta_e = 1$. $\beta\blacktriangledown = 0.069$ GPa with $\mathcal{S}_p^\star = 15$ %. $\eta = 0.039$ Pas and $u = 4.57$ m/s.

but with $H_0 = 2\,\mu$m, $A = H_0$ and $L_x = 0.1$ m. $\theta = 1$ both at inlet and outlet and hence flooded. The corresponding dimensionless density solution where the fitted expression is compared with the original Dowson & Higginson expression in Fig. B.6. From left to right, slight liquid compression occurs and full film solutions are achieved until the gap is expanding to a level where the liquid does not occupy the complete gap and cavitates. The pressure gradient is switched off and as a consequence, the Poiseuille flow is terminated and the lubricant is only transported by means of Couette flow. The fractional film content (θ) is rapidly decreasing further to the right in the domain. At the outlet boundary the lubricant is abruptly reformed into full film again. A significant difference in compression can be seen at the full film portion. Pressure solutions for the same conditions can be seen in Fig. B.7. The differences in pressure between the expressions are small, only 1.7 % even though the differences in compression (the solution variable) between the to compressibility expressions are substantial.

The dimensionless density solutions for the fitted and original Dowson & Higginson expression for a starved inlet with a fractional film content of 55 %, $\theta = 0.55$, can be seen in Fig. B.8. From the left, only Couette flow is present until the gap contracts sufficiently to compress the liquid and reformation into full film occurs abruptly. The reformation point

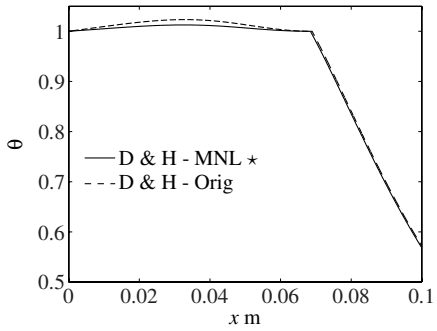

Figure B.6: Density solutions across the domain for the parabolic geometry with $H_0 = 2\,\mu$m and $A = H_0$ and boundary conditions $\theta_w = 1$ and $\theta_e = 1$. $\mathcal{S}_\theta^\star = 0.61$ %, $\eta = 0.04$ Pas and $u = 0.25$ m/s.

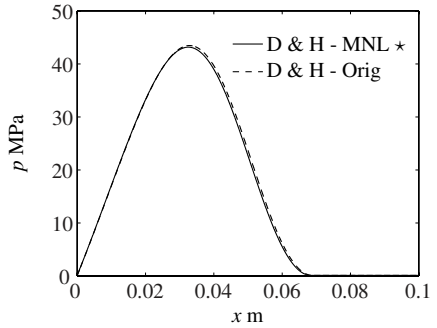

Figure B.7: Pressure solutions across the domain for the parabolic geometry with $H_0 = 2$ μm and $A = H_0$ and boundary conditions $\theta_w = 1$ and $\theta_e = 1$. $\mathcal{S}_p^\star = 1.7$ %, $\eta = 0.04$ Pas and $u = 0.25$ m/s.

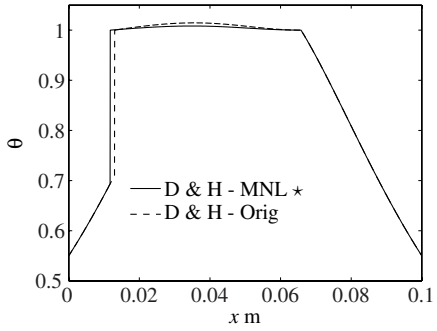

Figure B.8: Density solutions across the domain for the parabolic geometry with $H_0 = 2\,\mu$m and $A = H_0$ and boundary conditions $\theta_w = 0.55$ and $\theta_e = 1$. $\mathcal{S}_\theta^\star = 0.64$ %, $\eta = 0.04$ Pas and $u = 0.25$ m/s.

is slightly shifted between the two compressibility expressions. Further to the right the solutions mimics the earlier case with flooded inlet conditions. The film rupture boundaries

appears at the same locations. In the cavitated region the equation is hyperbolic because of the Couette term. Hence, no information is signaled from the downstream locations and consequently, upstream differencing is applied. The lack of influence from the downstream locations in the cavitated zones together with the the switch function give rise to this abrupt and somewhat unexpected reformation into full film. The corresponding pressure can be seen in Fig. B.9 where greater differences arise between the two Dowson & Higginson expressions, 7.4 %. Here, the expression for β =constant, taken for the fitted

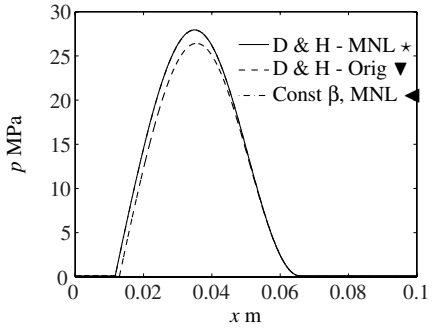

Figure B.9: Pressure solutions across the domain for the parabolic geometry with $H_0 = 2$ μm and $A = H_0$ and boundary conditions $\theta_w = 0.55$ and $\theta_e = 1$. ▼: $\mathcal{S}_p^\star = 7.4$ %, ◀: $\mathcal{S}_p^\star = 0.11$ %. $\eta = 0.04$ Pas and $u = 0.25$ m/s.

expression at $\theta = 1$ is added to the figure to show that the difference in solutions between this and the fitted Dowson & Higginson expression are negligible (overlapping lines) for these conditions. By inspecting Fig. B.1 it is evident that the fitted expression and the constant β expression are close in a pressure range of 0-100 MPa which is reflected in the results where the simulations are put so that the limits of hydrodynamic pressures are not exceeded. In Fig. B.10 the same physical conditions are applied as in Fig. B.9 and solutions are obtained for different values of β. Substantial differences in pressures are

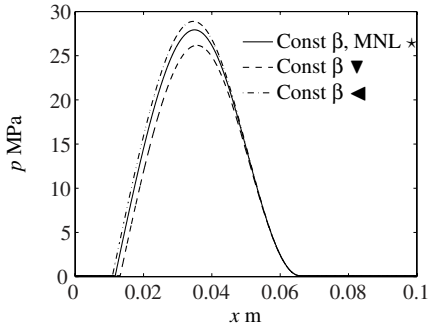

Figure B.10: Pressure solutions across the domain for the parabolic geometry with $H_0 = 2$ μm and $A = H_0$ and boundary conditions $\theta_w = 0.55$ and $\theta_e = 1$. $\beta = [\blacktriangledown 3.34/2, \blacktriangleleft 3.34 * 2]$ GPa with $\mathcal{S}_p^\star = [8.4, 4.8]$ %. $\eta = 0.04$ Pas and $u = 0.25$ m/s.

seen between the solutions indicating the importance of using a relevant value of the bulk

modulus for the lubricant to be simulated.

In Fig. B.11 a linearly converging film thickness is used with $H_0 = 1$ μm and $A = 0.25$ μm where the inlet film thickness is $H_0 + A$ and the outlet film thickness is H_0. To further

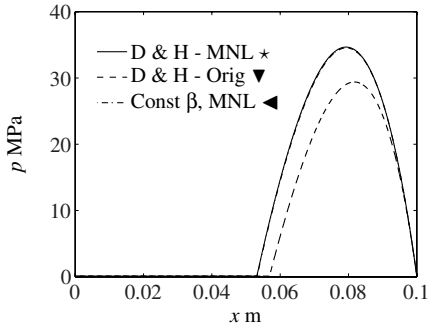

Figure B.11: Pressure solutions across the domain for the converging gap geometry with $H_0 = 1$ μm and $A = 0.25$ μm and boundary conditions $\theta_w = 0.85$ and $\theta_e = 1$. ▼: $\mathcal{S}_p^\star = 22$ %, ◀: $\mathcal{S}_p^\star = 0.54$ %. $\eta = 0.04$ Pas and $u = 0.25$ m/s.

study the effects of starvation, $\theta = 0.85$ is set at the inlet while ambient density is applied at the outlet. Also for this case the constant β expression produces results close to the mineral oil with a load difference of 0.54 %. However, the original Dowson & Higginson expression deviates significantly from the mineral oil with a load difference of 22 %. Great differences are also seen in Fig. B.12 for the different values of β.

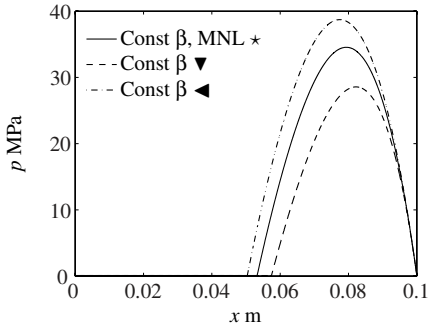

Figure B.12: Pressure solutions across the domain for the converging gap geometry with $H_0 = 1$ μm and $A = 0.25$ μm and boundary conditions $\theta_w = 0.85$ and $\theta_e = 1$. $\beta = [\blacktriangledown 3.34/2, \blacktriangleleft 3.34 * 2]$ GPa with $\mathcal{S}_p^\star = [25, 19]$ %. $\eta = 0.04$ Pas and $u = 0.25$ m/s.

The conditions at the inlet are significant in many aspects. We have seen that different compressibility models produce similar solutions in a pressure range reaching up to 50 MPa but become significantly different if the inlet is starved. Let us use the fitted Dowson & Higginson compressibility expression and focus on some geometrical aspects. In Fig. B.13 two sinusoidal waves applied on the left half of the geometry are shown. The inlet film thickness is H_0 and $H_0 + A$ respectively but the same at the end of the two sinusoidal waves. Pressure solutions for this geometry can be seen in Fig. B.14. The geometry

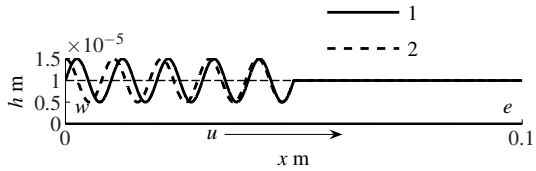

Figure B.13: Geometries with parallel gaps, two sinusoidal waves with a difference in frequency both at $(x < L/2)$ with $H_0 = 10\,\mu$m and $A = 0.5 * H_0$.

with the smaller film thickness at the inlet produces higher pressures. The results are somewhat unexpected since the geometry with a greater film thickness at the inlet is likely to cause a greater compression of the fluid. In this case however, the sinusoidal geometry is

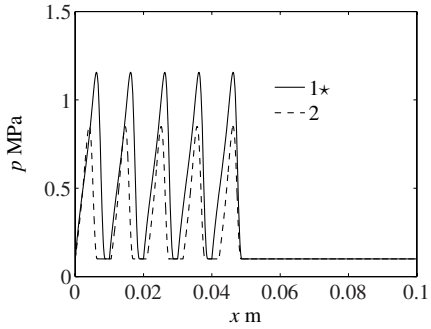

Figure B.14: Pressure solutions across the domain for the sinusoidal geometry at $(x < L/2)$ with $H_0 = 10\ \mu$m and $A = 0.4 * H_0$ m and boundary conditions $p_w = 1e+05$ and $p_e = 1e+05$ Pa. $\mathcal{S}_p^\star = 35$ %. $\eta = 0.04$ Pas and $u = 0.25$ m/s.

able to pull a larger amount of fluid into the domain up to the point where the gap expands and the fluid cavitates. The non-dimensional density at the location of the first sinusoidal wave is shown in Fig. B.15. It can be seen that the fluid tends to get more compressed for geometry 2 until the earlier diverging gap leads to an earlier cavitation which affect the compression.

If the same sinusoidal waves as in Fig. B.14 are squared, we get a film thickness as in Fig. B.16. Here the smallest film thickness is H_0. The pressure results can be viewed in Fig. B.17. If the inlet is flooded the geometry 1 cavitates throughout the domain producing zero load carrying capacity. Since the inlet film thickness for the geometry 2 is larger than H_0 some fluid compression can occur and the pressure will rise across the domain producing load carrying capacity. If the geometry is pressurized, it is now possible even for the sin geometry to produce a pressure build-up.

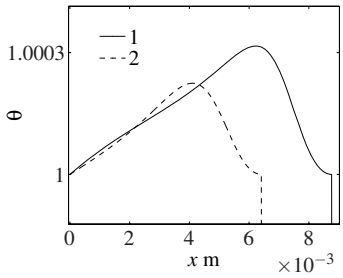

Figure B.15: Density solutions across the domain for the sinusoidal geometry at $(x < L/2)$ with $H_0 = 10\,\mu$m and $A = 0.5 * H_0$ and boundary conditions $p_w = 1e+05$ and $p_e = 1e+05$ Pa. $\eta = 0.04$ Pas and $u = 0.25$ m/s.

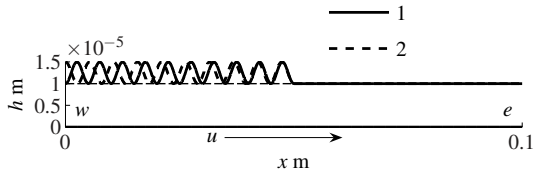

Figure B.16: Geometries with parallel gaps, two squared sinusoidal waves with a difference in frequency both at $(x < L/2)$ with $H_0 = 10\,\mu$m and $A = 0.5 * H_0$.

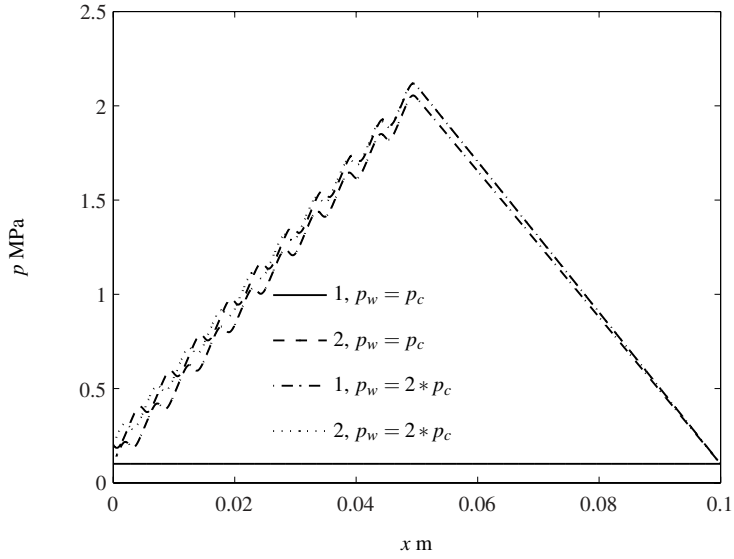

Figure B.17: Pressure solutions across the domain for the $\cos^2$ at $(x < L/2)$ modified step geometry with $H_0 = 10\,\mu$m and $A = 0.5 * H_0$ and boundary conditions $p_w = 2 * 10^5$ and $p_e = 10^5$ Pa. $\eta = 0.04$ Pas and $u = 0.25$ m/s.

B.5 Conclusions

A generalized Reynolds equation accommodating for an arbitrary compressibility relation and cavitation has been derived. It has been shown that different compressibility models can produce significantly different results in a hydrodynamic pressure range. Load carrying capacity is especially sensitive to the type of compressibility relation used if the inlet is starved. This indicates the need of employing realistic density-pressure relations. To produce better predictions of cavitation regions, fractional film content and pressure, more physical variables that are put dependent such as viscosity might be needed. Surface roughness close to the inlet has been shown to have important effects on load carrying capacity.

Paper C

Submitted for publication in Tribology International (2005)

Rough Surface Flow Factors in Full Film Lubrication based on a Homogenization Technique

F. Sahlin, A. Almqvist, R. Larsson, S. Glavatskih

Luleå University of Technology, Division of Machine Elements, Luleå, SE-971 87 Sweden

Abstract

This paper describes a method to compute flow factors compensating for an arbitrary surface roughness in compressible hydrodynamic lubrication based on a homogenization technique. Reynolds equation is used as the governing equation and the two-scale expansion involved in the homogenization process enables the local roughness scale to be treated separately from the global geometry scale. With this method it is possible to compute flow factors for for any deterministic roughness. Measured two-dimensional surface profiles are used as examples. By utilizing a randomization technique it is shown that profiles having the same Abbot-Firestone bearing ratio also have the same flow factors, providing an efficient classification of surfaces in hydrodynamic two-dimensional contacts. Flow factors are computed for the surface profiles and solutions for global problems are obtained and compared with the corresponding smooth solutions.

C.1 Introduction

It is known that the surface roughness affects the performance in various ways in a lubricated contact. Even if the surfaces are smooth on a macroscopic level, asperities on a microscopic level will affect the overall performance in terms of pressure build-up, film thickness and friction. As computer performance increases the theoretical simulations of lubricated contacts become more focused on treating the roughness. Since the width of a typical asperity is much smaller than the total length of the contact, deterministic computations become difficult even with today's computer power. Thus it is desirable to find a way to reduce the number of degrees of freedom and still treat the effects from the surface roughness.

Stochastic theories such as those reported by Tzeng and Saibel [24] for one-dimensional transversal roughness and by Christensen [25] for longitudinal and transversal roughness are early approaches to deal with roughness effects in hydrodynamic lubrication. Elrod [26] performed a multiple-scale analysis for two-dimensional roughness where he assumed that the characteristic wavelength is small enough for the approach to be permitted. Patir and Cheng [27, 28] derived a method where the Reynolds equation is rewritten in terms of control volume averaged flow factors, applicable to any roughness structure. The flow factors are determined empirically by simulating model bearings with surfaces having certain roughness statistics. They showed that the ratio of x and y correlation lengths plays an important role in characterizing the flow factors. A lot of work has been carried out by following the footsteps of the early flow factor approach by Patir and Cheng. More recently, variants of the Patir and Cheng flow factor computations include Lunde and Tønder [29] where the use of boundary conditions can be avoided, Letalleur et al. [30] where flow factors for sinusoidal surfaces are studied and can be retrieved analytically near contact, Wang et al. [31] who use the Patir and Cheng approach and incorporate a contact model and extend the problem into a mixed EHD model, Harp and Salant [32] who use the flow factor model and formulate the flow problem to treat inter-asperity cavitation.

Recent work has paid much attention to homogenization techniques when treating the surface roughness. The flow problem is decoupled into two problems; the homogenized problem on the macroscopic scale describing the bearing geometry, and the local (or cell) problem on the microscopic scale describing the roughness. Examples of such work include Kane and Bou-Said [33] who compare homogenization and direct techniques, Jai and Bou-Said [34] who compare homogenization and averaging techniques and Bayada et al. [35] who use a homogenization technique which also treats the concept of cavitation.

In this work we present an approach to generate flow factors compensating for the surface roughness in the full film hydrodynamic regime using the homogenized results of the compressible Reynolds equation presented by Almqvist and Dasht [36]. The flow factors can be computed for an arbitrary periodic two- or three-dimensional roughness which permits the use of measured surface topographies of real surfaces. In the current work two-dimensional surface roughness is considered and as a numerical test case, four measured surface profiles are used. Surface profiles are also generated artificially in a randomized way but with the the same Abbot-Firestone bearing ratio as the original measured surfaces.

C.2 Theory

The Reynolds equation is well suited for solving fluid film flows in e.g. bearings. However, to simulate a complete bearing including the surface roughness is not feasible because of the amount of degrees of freedom required to resolve the roughness. In this section a way to separate the effects of the surface roughness from the effects of the global geometry of the bearing is described. Let us assume that a surface can be quite well represented by using two geometry scales where one scale is much smaller than the other. With this in mind we can express the total film thickness as

$$h(x) = h_0(x) + h_1(x/\varepsilon), \quad \varepsilon > 0 \tag{C.1}$$

where h_0 represents the global geometry scale and h_1 the roughness scale which is an arbitrary periodic function expressed in one period with a wavelength parameter ε. For this condition, the compressible Reynolds equation is homogenized by Almqvist and Dasht in [36]. The homogenization process involves an asymptotic two-scale expansion for the solution variable and letting $\varepsilon \to 0$. This permits the local and the global problems to be treated separately. Since the global problem do not involve any rapid oscillations it requires less numbers of degrees of freedom to be accurately resolved.

The above discussion will be revisited later but consider now a measured two-dimensional surface profile $r(x)$ with zero mean value. In the hydrodynamic contact the profile and related measures are shown in Fig. C.1. Now the film thickness of the lubricated contact can

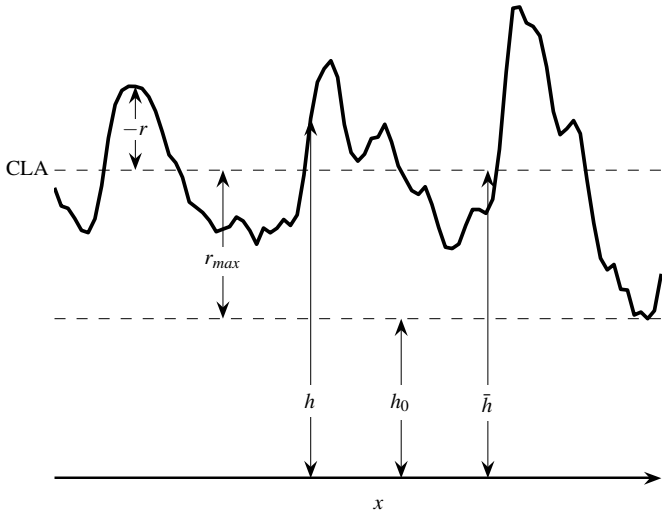

Figure C.1: Film thickness and related parameters.

be expressed as

$$h(x) = \bar{h} - r. \tag{C.2}$$

The film thickness is constant in time and the stationary compressible Reynolds equation constitutes the basis in this work, viz.

$$\frac{d}{dx}\left(\frac{\rho h^3}{12\eta}\frac{dp}{dx}\right) = \frac{u}{2}\frac{d(\rho h)}{dx}, \tag{C.3}$$

where p is pressure, η viscosity and ρ is the density. It is convenient to express the equation in terms of density as dependent variable so we define the dimensionless density as

$$\theta = \frac{\rho}{\rho_c} \tag{C.4}$$

where ρ_c is the density at ambient pressure $p = p_c$. We assume that $p = p(\theta)$ and hence it is possible to apply the chain rule on the pressure gradient, i.e.,

$$\frac{dp}{dx} = \frac{dp}{d\theta}\frac{d\theta}{dx}. \tag{C.5}$$

Substituting the expression for the pressure gradient and θ into the Reynolds equation yields:

$$\frac{d}{dx}\left(\frac{\theta h^3}{12\eta}\frac{dp}{d\theta}\frac{d\theta}{dx}\right) = \frac{u}{2}\frac{d(\theta h)}{dx}. \tag{C.6}$$

Assuming further that the bulk modulus, defined as

$$\beta = \theta\frac{dp}{d\theta}, \tag{C.7}$$

can be treated as a constant yields the following expressions relating pressure to density:

$$p = p_c + \beta\ln(\theta) \tag{C.8}$$

and the equivalent expression relating density to pressure:

$$\theta = \exp\left(\frac{p - p_c}{\beta}\right). \tag{C.9}$$

Note that the constant bulk modulus gives rise to an exponential expression for $\theta(p)$ which is an acceptable compressibility relation for a limited pressure range, see [37] for a more comprehensive discussion regarding this matter. Under this condition Eq. (C.6) can be written:

$$\frac{d}{dx}\left(h^3\frac{d\theta}{dx}\right) = \Lambda\frac{d(\theta h)}{dx} \tag{C.10}$$

where $\Lambda = 6\eta u/\beta$. To obtain a homogenized equation in a more general form independent of Λ we define the following dimensionless parameters:

$$H = \frac{h}{\bar{h}}; \quad G = \frac{-r}{r_{max}}; \quad \alpha = \frac{r_{max}}{\bar{h}}; \quad \bar{x} = \frac{6\eta u x}{\beta(r_{max})^2}; \quad \bar{p} = \frac{p}{p_c}. \tag{C.11}$$

Also let $r = r(\xi)$ which now corresponds to h_1 in Eq. (C.1) where $\xi = x/\varepsilon$. Dividing Eq. (C.2) by $\bar{h}$ and using the above expressions the dimensionless film thickness equation can be written as

$$H_\alpha(\xi) = 1 + \alpha(G(\xi) - 1), \quad 0 \le \alpha < 1, \tag{C.12}$$

where the subscript indicates that α is a parameter. As α goes from zero to one, the clearance h goes from zero to infinity. It should be noted that the mean value of H always equals unity and as the α decreases, H becomes smoother and equals to unity for $\alpha = 0$. Substituting H_α, $\bar{p}$ and $\bar{x}$ into Eq. (C.10) the dimensionless form of the equation becomes:

$$\frac{d}{d\bar{x}}\left(H_\alpha^3\frac{d\theta}{d\bar{x}}\right) = \frac{d(\theta H_\alpha)}{d\bar{x}}. \tag{C.13}$$

The corresponding homogenized equation (see Almqvist and Dasht [36]) yields:

$$\frac{d}{d\bar{x}}\left(\phi_{x\alpha}\frac{d\theta}{d\bar{x}}\right) = \frac{d}{d\bar{x}}\left(\phi_{s\alpha}\theta\right), \tag{C.14}$$

where

$$\begin{aligned}\phi_{x\alpha} &= \int_0^1 H_\alpha^3(\xi)\left(1+\frac{\partial\psi_\alpha}{\partial\xi}\right)d\xi \quad \text{and}\\ \phi_{s\alpha} &= \int_0^1 \left(H_\alpha(\xi) - H_\alpha(\xi)^3\frac{\partial\chi_\alpha}{\partial\xi}\right)d\xi.\end{aligned} \tag{C.15}$$

ψ and χ are solutions to the local problems, i.e. the local roughness scales which are given by

$$\begin{aligned}\frac{\partial}{\partial\xi}\left(H_\alpha^3\frac{\partial\psi_\alpha}{\partial\xi}\right) &= -\frac{\partial\left(H_\alpha^3\right)}{\partial\xi} \quad \text{and}\\ \frac{\partial}{\partial\xi}\left(H_\alpha^3\frac{\partial\chi_\alpha}{\partial\xi}\right) &= \frac{\partial H_\alpha}{\partial\xi}.\end{aligned} \tag{C.16}$$

The dimensionless Reynolds equation has lead to the local problems being independent of Λ. Since the local problems are solved at a unit cell domain, physical spatial properties of the roughness are diminished which explains the choice of non-dimensionalization of x in Eq. (C.11). Simply speaking, the influence of $\bar{x}$ disappears in the solutions of the local problems.

The dimensionless film thickness Eq. (C.12) has led to the homogenized equation being independent of x but dependent on the parameter α. This permits the local problems to be solved for $0 < \alpha \leq 1$ producing flow factors ϕ_x and ϕ_s as functions of α which add the contribution from different roughness $G(\xi)$ to a global coarse homogenized problem. With a database of previously computed flow factor the non-dimensional homogenized equation can be directly solved on the non-dimensional coordinate $\bar{x}$ to achieve the solution θ. Instead of using the somewhat inconvenient definition of $\bar{x}$ the dimensionless homogenized equation can be directly scaled into dimensional form

$$\frac{d}{dx}\left(\phi_x(x)\bar{h}(x)^3\frac{d\theta}{dx}\right) = \frac{d}{dx}\left(\phi_s(x)\bar{h}(x)\Lambda\theta\right), \tag{C.17}$$

where ϕ_x and ϕ_s are retrieved from the parametrized $\phi_{x\alpha}$ and $\phi_{s\alpha}$ by e.g. table look-up to become functions of x. This equation could be compared with the one derived by Patir and Cheng [28] but with the use of different flow factors ϕ_x and ϕ_s.

C.3 Results

C.3.1 The Effect of ε

In the two-scale approach involved in the homogenization process the wavelength measure ε of the local roughness scale is set to approach zero. This would correspond to a deterministic solution for a geometry with a periodic roughness wavelength approaching zero. The thin film approximation involved when solving the Reynolds equation only permits

solving a problem with a large width to height roughness ratio. However, to verify the homogenized solution, a corresponding deterministic solution could be obtained where the roughness wavelength decreases to a finite level. The deterministic solution should then approach the homogenized. Consider the film thickness equation

$$h = h_0 + A\sin\left(\frac{2\pi}{\varepsilon L_x}\right) \tag{C.18}$$

where h_0 is a convergent gap and $A = \min(h_0)/10$. This film thickness is shown in Fig. C.2 with sinusoidal waves of different wavelengths. Deterministic and homogenized pressure

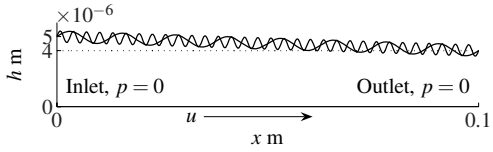

Figure C.2: A convergent gap geometry model with sinusoidal roughness with $\varepsilon = 2^{-5}$ and 2^{-3}.

solutions for this geometry are shown in Fig. C.3. It can be seen that the deterministic

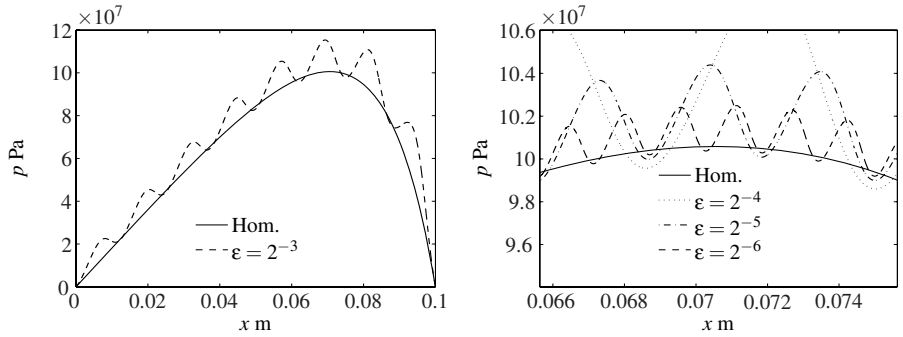

(a) Full domain (b) Magnified area

Figure C.3: Pressure distribution along a converging gap with sinusoidal roughness for the homogenized and deterministic solutions.

solutions approach the homogenized as the wavelength decreases. Good correspondence between the deterministic and the homogenized solutions is achieved for a finite value of the wavelength. This motivates the treatment of the limit $\varepsilon \to 0$ in the homogenization process.

C.3.2 Flow Factors

In this section four measured two-dimensional surface topographies are used in the numerical examples. The machining process applied to the surfaces and some of their surface parameters are given in Table C.1. It can be seen that surface *A* differs a lot from the other surfaces in R_a value. Surfaces *B* and *D* are quite similar but differ significantly in skewness. The Abbot-Firestone bearing ratio for the four profiles can be seen to the left in

Table C.1: Data for the four original surface profiles.

#	Machining	R_a	R_q	SK	K
A	Unidirectional ground	0.93	5.0	-0.99	4.3
	+ Phosphated and dephosphated				
B	Unidirectional ground	0.29	1.2	-0.49	3.3
C	Unidirectional ground	0.13	0.58	-0.010	3.6
	+ 3 x chemically deburred				
D	Unidirectional ground	0.37	1.6	0.032	3.0
	+ shot-peened				

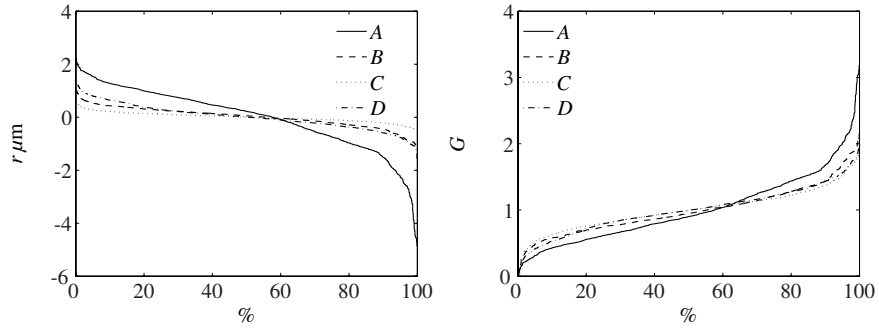

Figure C.4: Abbot-Firestone bearing ratio for the surfaces in dimension (left) and dimensionless (right).

Fig. C.4. This cumulative height distribution contains all height information about a surface such as for example R_a, R_q, skewness and kurtosis but no spatial information. Since the simulations will consider the dimensionless surface roughness we show the cumulative height distribution in terms of G, for clarity, to the right in Fig. C.4 where the mean value of G equals unity. With this dimensionless representation the absolute height values are insignificant and only the shape of the Abbot-Firestone bearing ratio is relevant. The results to be discussed are based on these dimensionless height distributions.

The surface measurements consist of 512 points equally spaced and distributed on a length of 4.2×10^{-4} m. To compute the flow factors, see Eq. (C.15), the number of degrees of freedom of the measurement has to be increased. The computational grid has to be sufficiently dense in order to resolve the roughness on a cell.

For this reason extra grid nodes are linearly interpolated between the points of the surface measurements, Fig. C.5. Because of the linear interpolation no information is added or removed and the surface representation will become identical to that of the the measurements, only more degrees of freedom are added to the solution process. The demand for more degrees of freedom is illustrated in Fig. C.6(a) where the flow factors ϕ_s are shown for surface A as functions of the parameter α for increasing number of grid nodes N. Solutions from 50 values of α, equally spaced between $\alpha = 10^{-9}$ and $\alpha = 1 - 10^{-9}$ are used[1]. The dashed line represents the original profile and it is seen that the flow factors

[1]Mechanical contact occurs for $\alpha = 1$

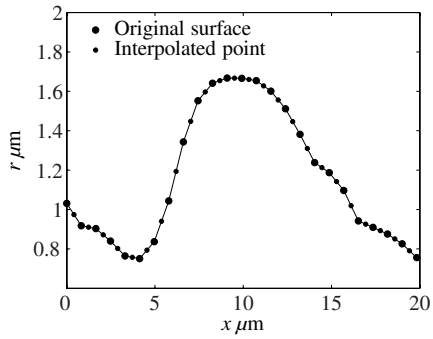

Figure C.5: A small part of the original surface and linear interpolation with one point.

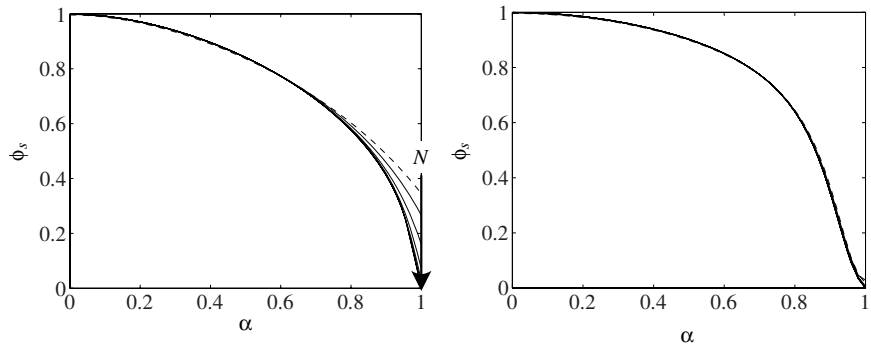

(a) Surface *A* (b) Surface *B*

Figure C.6: Flow factor with increasing number of interpolation points where dashed line represents the original surface with 2^9 points and highest resolution is $N = 2^{16}$. A total of 8 curves are shown in each plot

become more and more sensitive to grid resolution as α approaches unity. Because of the way that H is non-dimensionalized, the mean value of H is always unity and the shape of H becomes smoother as α approach zero which means that the demand on resolution decreases. Particularly, at the extreme of $\alpha = 0$ the local problem can be solved analytically. The same conditions are applied for surface B in Fig. C.6(b). It is clear that this profile is less sensitive to grid resolution than surface A. To display the change of the flow factors as the grid spacing is reduced, we define the difference in solutions between two consecutive grid spacings δ and and its double spacing 2δ respectively as

$$\widehat{\phi}^{\delta} = \left| \phi^{2\delta} - \phi^{\delta} \right| \tag{C.19}$$

where $\widehat{\phi}$ is taken at some value of α. A visualization for convergence measure is seen in Fig. C.7. The linear behavior for the convergence in flow factor for $\alpha = 0.49$ at higher resolutions indicates that the error reduction is in agreement with the effective order of the discretization scheme which is not that obvious for α close to unity. However, the flow factors for a film thickness approaching zero are somewhat uncertain regardless resolution since the hydrodynamic regime is to some extent violated. It can also be seen that the

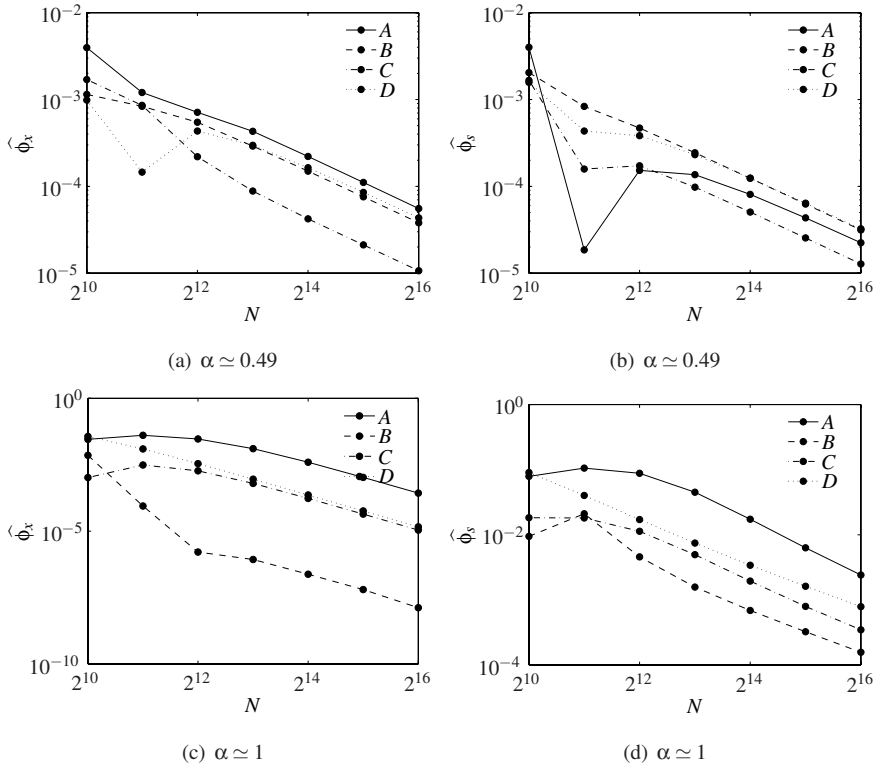

(a) $\alpha \simeq 0.49$ (b) $\alpha \simeq 0.49$

(c) $\alpha \simeq 1$ (d) $\alpha \simeq 1$

Figure C.7: Flow factor convergence as a function of spatial resolution.

convergence rate for surface A is generally smaller than for the other surfaces.

C.3.3 Surface Classification

It is desirable to find classes of surface roughness that affect the pressure in a hydrodynamic contact similarly, i.e. having the same flow factors. In the Abbot-Firestone bearing ratio all surface height parameters are known but no information about spatial parameters is revealed. In this work the Abbot-Firestone bearing ratio is Considered as a suitable tool for surface classification. To do this the Abbot-Firestone bearing ratios from the original surface profiles are used and the points at discrete levels of the curves are spatially distributed in a random way to produce surfaces having the same Abbot-Firestone bearing ratio. In order not to violate the thin film approximation, the distribution of points is controlled in certain ways. A fully randomized surface could have the have highest and lowest points as neighbors. This is accomplished by introducing some rules so that points are allowed to be positioned spatially close to existent points at a higher height level. If that is not possible, new peaks are formed from where points can be positioned at a lower height level. Hence, the points are not fully randomly distributed. This is because the profiles would violate the thin film approximation, with the possibility of highest and lowest points being neighbors. Flow factors for the original and five random surfaces are shown in Fig. C.8. At the top two figures the original measured profiles with $N = 2^9$ are used. The

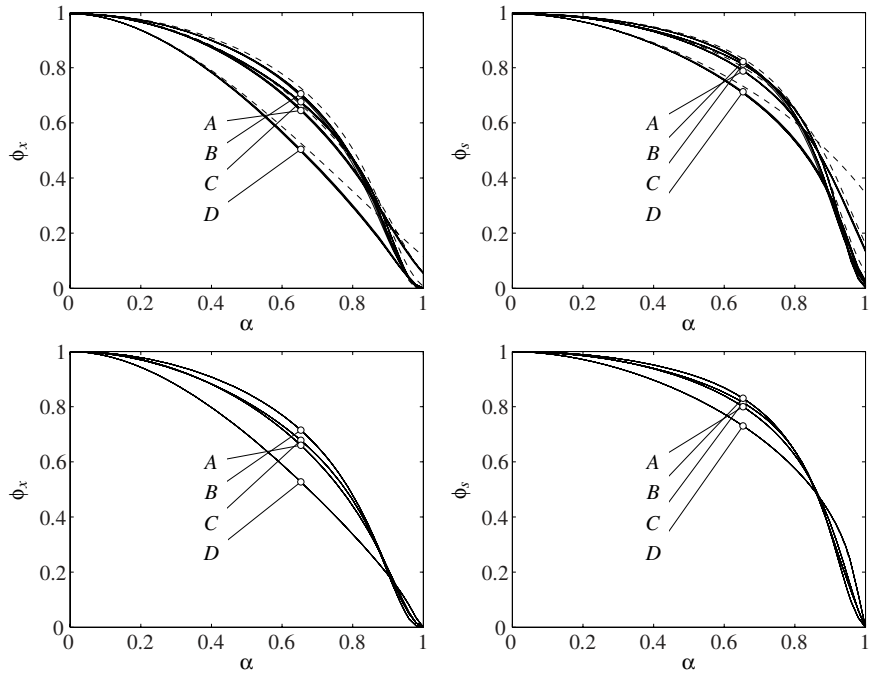

Figure C.8: Flow factors against α for all surfaces. The resolution is $N = 2^9$ top and $N = 2^{16}$ bottom. For each original surface (dashed), five randomizations of that surface are also plotted.

randomized profiles are fairly well clustered together but the original profiles differ significantly. As discussed before, more degrees of freedom than those of the original profiles need to be introduced, especially for α close to unity. At the bottom two figures interpolation is applied where $N = 2^{16}$. All surfaces having the same Abbot-Firestone bearing ratio coincide and it is clear that for a sufficiently resolved profile, the Abbot-Firestone bearing ratio is by itself determining the result. Hence the Abbot-Firestone bearing ratio holds the information necessary to predict the influence of surface roughness on the flow factors introduced by the homogenization process.

To get a better idea of the deviation between the 6 profiles, i.e., the five randomized profiles and the original profile, the standard deviation of ϕ_x is computed for each value of α, Fig. C.9. The standard deviation for each surface reaches a maximum at α close to one. The same applies for standard deviations of ϕ_s but with a maximum of less than 1.2×10^{-6}. The maximum standard deviation decreases as N increases which is obvious from Fig. C.10. This confirms that the Abbot-Firestone bearing ratio acts as a good classification. To confirm that the maximum standard deviation is small enough, the homogenized equation is solved for a dimensional converging gap geometry where the smallest film thickness is represented by $\alpha = 0.99$ and the largest film thickness by $\alpha = 0.6$ for all four surfaces. This is in order to cover a range where the standard deviations of flow factors are the largest for all four surfaces, see Fig. C.9. The load carrying capacity is then used to monitor the total error. Each surface (A,B,C,D) is interpolated to $N = 2^{16}$ grid nodes and the standard deviation for load carrying capacity was computed. For all sur-

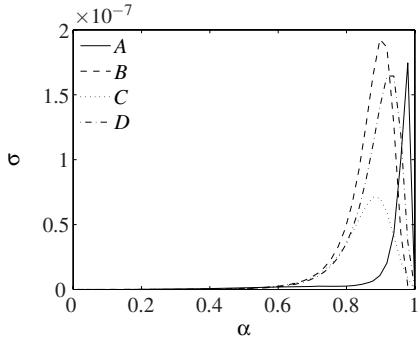

Figure C.9: Standard deviations of ϕ_x for the random and original profiles where $N = 2^{16}$.

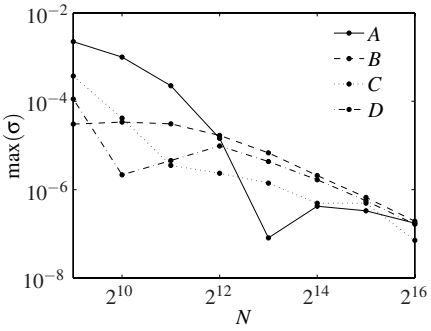

Figure C.10: Maximum standard deviations of ϕ_x in the α–range.

faces, the value of this measure was found to be less than 0.1 % of the mean load carrying capacity.

C.3.4 Application Examples

Some dimensional bearing examples will be shown where the computed flow factors are used to solve the homogenized problem. The non-dimensional flow factors for the original profiles are used and scaled into dimensional ones (see Section C.2) allowing the homogenized equation to be solved for the dimensional spatial domain. The flow factors needed for the corresponding film thickness are discretely retrieved by cubic spline interpolation from the computed flow factors. The film thickness notations are in terms of the mean nominal separation $\bar{h}$. In all simulations, the domain length in the x-direction $\mathcal{L}_x = 0.1$ m, $\eta = 0.14$ Pas, $\beta = 10^9$ GPa, $u = 1$ m/s, $p_c = 10^5$ Pa which also are the inlet and outlet Dirichlet boundary conditions. It should be noted that side leakage is not considered since the one-dimensional Reynolds equation is used and therefor, the load carrying capacity becomes greater than for two-dimensional problems.

To verify if the local problems are sufficiently resolved in terms of N to produce sufficiently accurate solutions to the dimensional homogenized problems we compute the convergence in the load carrying capacity between two consecutive grid spacings δ and its

double spacing 2δ respectively as

$$\widehat{W}^{\delta} = \frac{\left|W^{\delta} - W^{2\delta}\right|}{W^{\delta}} \tag{C.20}$$

where the load carrying capacity is computed as

$$W = \int_0^{L_x} p \, \mathrm{d}x. \tag{C.21}$$

The load convergence for the converging cap with $\min(\bar{h}) = 5\ \mu$m and $\max(\bar{h}) = 6\ \mu$m is shown in Fig. C.11 from where it can be seen that the critical limit is $N = 2^{11}$ and the

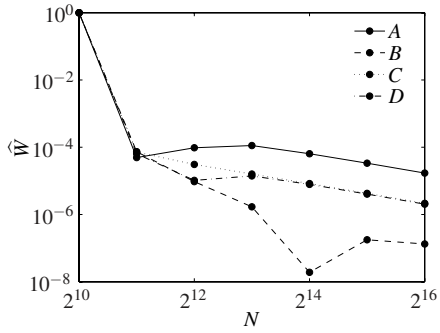

Figure C.11: Load convergence as a function of grid resolution for a converging gap. $\widehat{W} < 1.8 \times 10^{-5}$ for all surfaces at highest resolution with $N = 2^{16}$.

change at the highest resolution is considered as sufficiently small. Thus, $N = 2^{16}$ is the resolution used when displaying all dimensional results.

The minimum global film thickness $\min(h_0(x))$ is used as a solution variable, determined in order to achieve force balance for a given load.

Consider a converging gap geometry with $\max(h_0(x)) = \min(h_0(x)) + 1\ \mu$m. In Fig. C.12 the minimum value of h_0 is plotted as a function of load carrying capacity for the rough profiles and a smooth, denoted S. The ordering of the minimum film thickness follows the ordering of R_a values for the roughness profiles, with surface A standing for the smallest film thicknesses and the smooth S for the largest, respectively. It is also clear from the figure that as the film thickness increases the influence of roughness decreases.

Now consider a parabolic geometry shown in Fig. C.13. Since atmospheric pressure is applied at the boundaries, cavitation is likely to occur at some point in the diverging part. For this case we use the approach of treating cavitation by Vijayaraghavan and Keith [20]. They use a Reynolds equation in a different form than presented here. This means that the homogenization process does not apply for that equation. However, since the equation only differs in a switch function applied to the Couette term the equation is identical to the one which is homogenized in the flooded region where the switch function equals one. If Eq. (C.17) is modified by the switch function to treat cavitation, the global problem will treat cavitation but not the local problem. This leads to vanishing of ϕ_x at cavitation but the influence from ϕ_s will remain. pressure distribution obtained from the modified homogenized equation for surface A is given in Fig. C.14. Pressure is rising when the

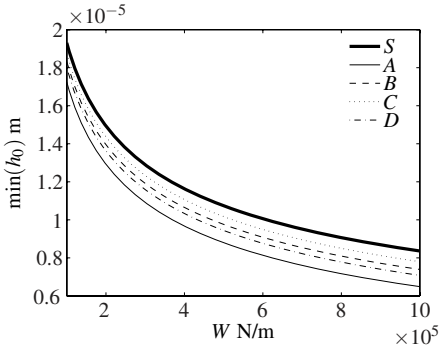

Figure C.12: The minimal film thickness as a function of load carrying capacity for the converging gap geometry.

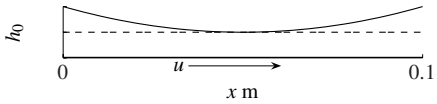

Figure C.13: A parabolic geometry with $\max(h_0) = \min(h_0) + 1 \times 100\,\mu$m.

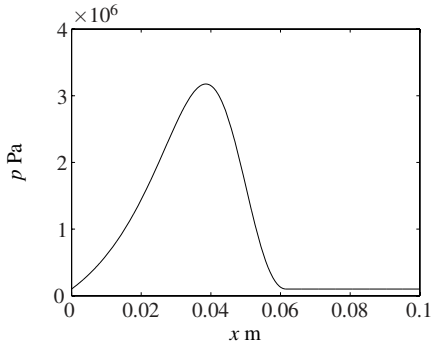

Figure C.14: Pressure across the domain for the parabolic geometry when surface A is used. $W = 100$ kN/m.

gap is converging and in the diverging part where $x \approx 0.07$ m cavitation occurs. The effect of surface roughness on film thickness h_0 as a function of load carrying capacity is shown in Fig. C.15. As for the converging gap geometry the rough surfaces give smaller film thickness h_0 compared to the smooth geometry. And the same order in which rough surfaces affect h_0 applies here too.

C.4 Conclusions

In this paper we consider a homogenization technique for the compressible Reynolds equation. The approach involves an asymptotic two-scale expansion of the film thickness. For

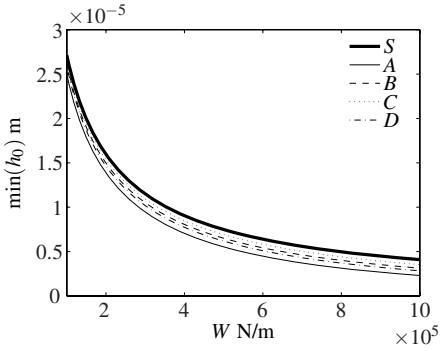

Figure C.15: The minimal film thickness as a function of load carrying capacity for the parabolic geometry.

a lubrication problem involving rough surfaces, this method provides a mathematical approach that separates the hydrodynamic effects at the local scale, representing the surface roughness, from the hydrodynamic effects at the global scale, representing the bearing geometry. The conclusions are as follows:

- A novel method of computing dimensionless flow factors for arbitrary surface roughness using a homogenization technique has been developed.
- The method provides flow factors for arbitrary global geometries within the full film regime.
- It has been shown that different profiles having the same Abbot-Firestone bearing ratio give the same flow factors, thus providing an efficient classification system for surfaces intended to operate in full film lubrication.

Bibliography

[1] F. P. Snegovskii and N. G. Bulyuk. Study of lubrication of sliding bearings with microgrooves on the sliding shafts. *Trenie i Iznos*, 4(2):322–329, 1983.

[2] N. G. Bulyuk. Thermal analysis of sliding bearing with micro-channels on the shaft friction surface. *Trenie i Iznos*, 9(5):1007–1018, 1988.

[3] G. Ryk, Y. Kligerman, and I. Etsion. Experimental investigation of laser surface texturing for reciprocating automotive components. *Tribology Transactions*, 45(4):444–449, October 2002.

[4] S.B. Glavatskih, D.M.C. McCarthy, and I. Sherrington. Hydrodynamic performance of a thrust bearing with micro-patterned pads. *Accepted for publication in Tribology Transactions*, 2005.

[5] I. Etsion and G. Halperin. A laser surface textured hydrostatic mechanical seal. *Tribology Transactions*, 45(3):430–434, July 2002.

[6] I. Etsion A. Ronen and Y. Kligerman. Friction-reducing surface-texturing in reciprocating automotive components. *Tribology Transactions*, 44(3):359–366, July 2001.

[7] V. Brizmer, Y. Kligerman, and I. Etsion. A laser textured parallel thrust bearing. *Tribology Transactions*, 46:397–403, July 2003.

[8] M. Arghir, N. Roucou, M. Helene, and J. Frene. Theoretical analysis of the incompressible laminar flow in a macro-roughness cell. *Journal of Tribology*, 125:309–318, April 2003.

[9] F. Sahlin. Cfd-analysis of hydrodynamic lubrication of textured surfaces. Master's thesis, Luleå University of Technology, 2003. See also URL http://epubl.luth.se/1402-1617/2003/index.shtml.

[10] Cfx-4 documentation. AEA Technology.

[11] J. H. Ferziger and M. Perić. *Computational Methods For Fluid Dynamics*. Springer, third edition, 2002.

[12] P. N. Shankar and M. D. Deshpande. Fluid mechanics in the driven cavity. *Annu. Rev. Fluid Mech.*, 32:93–136, 2000.

[13] B. Jakobsson and L. Floberg. The finite journal bearing, considering vaporization. Technical Report 190, Institute of Machine Elements, Chalmers University of Technology, Gothenburg, Sweden, 1957.

[14] L. Floberg. The two-groove journal bearing, considering cavitation. Technical Report 231, Institute of Machine Elements, Chalmers University of Technology, Gothenburg, Sweden, 1960.

[15] L. Floberg. Lubrication of two cylinder surfaces, considering cavitation. Technical Report 232, Institute of Machine Elements, Chalmers University of Technology, Gothenburg, Sweden, 1961.

[16] L. Floberg. On hydrodynamic lubrication with special reference tu sub-cavity pressure and number of streamers in cavitation regions. *Acta Polytechnica Scandinavica*, (19), 1965.

[17] L. Floberg. Sub-cavity pressure and number of oil streamers in cavitation regions with special reference to the infinite journal bearing. *Acta Polytechnica Scandinavica*, (37), 1968.

[18] H. G. Elrod. A caviatation algorithm. *Journal of Tribology*, 103:350–354, jul 1981.

[19] H. G. Elrod and M. L. Adams. A computer program for cavitation and starvation problems. *Cavitation and Related Phenomena in Lubrication*, pages 37–42, 1975.

[20] D. Vijayaraghavan and T. G. Keith Jr. Development and evaluation of a cavitation algorithm. *STLE Tribology Transactions*, 32(2):225–233, Apr 1989.

[21] D. Vijayaraghavan and T. G. Keith Jr. An efficient, robust, and time accurate numerical scheme applied to a cavitation algorithm. *Journal of Tribology*, 112(1), Jan 1990.

[22] D. Dowson and G. R. Higginson. *Elastohydro-Dynamic Lubrication*. Oxford, 1966.

[23] R. Tuomas and O. Isaksson. Compressibility of oil/refrigerant lubricants in elastohydrodynamic contacts. To be published in *Journal of Tribology*.

[24] S. T. Tzeng and E. Saibel. Surface roughness effect on slider bearing lubrication. *SLE Trans.*, 10:334–338, 1967.

[25] H. Christensen. Stochastic models for hydrodynamics lubrication of rough surfaces. *Int. J. of Mech. Eng.*, 184(55):1013–1022, 1970.

[26] H.G. Elrod. A general theory for laminar lubrication with reynolds roughness. *Journal of Tribology*, 101(1):8–14, Jan 1979.

[27] N. Patir and H. S. Cheng. An average flow model or determining effects of three-dimensional roughness on partial hydrodynamic lubrication. *Journal of Tribology*, 100:12–17, 1978.

[28] N. Patir and H. S. Cheng. Application of average flow model to lubrication between rough sliding surfaces. *Journal of Tribology*, 101:220–230, 1979.

[29] L. Lunde and K. Tonder. Pressure and shear flow in a rough hydrodynamic bearing, flow factor calculation. *Journal of Tribology*, 119:549–555, 1997.

[30] N. Letalleur, F. Plouraboue, and M. Prat. Average flow model of rough surface lubrication: Flow factors for sinusoidal surfaces. *Journal of Tribology*, 124:539–546, 2002.

[31] Q. J. Wang, D. Zhu, H. S. Cheng, T. Yu, X. Jiang, and S. Liu. Mixed lubrication analyses by a macro-micro approach and a full-scale mixed ehl model. *Journal of Tribology*, 126(1):81–91, Jan 2004.

[32] S. R. Harp and R. F. Salant. An average flow model of rough surface lubrication with inter-asperity cavitation. *Journal of Tribology*, 123(1):134–143, 2001.

[33] M. Kane and B. Bou-Said. Comparison of homogenization and direct techniques for the treatment of roughness in incompressible lubrication. *Journal of Tribology*, 126(4):733–737, oct 2004.

[34] M. Jai and B. Bou-Said. A comparison of homogenization and averaging techniques for the treatment of roughness in slip-flow-modified reynolds equation. *Journal of Tribology*, 124(2):327–335, April 2002.

[35] Guy Bayada, Sebastien Martin, and Carlos Vazquez. An average flow model of the reynolds roughness including a mass-flow preserving cavitation model. *Journal of Tribology*, 127(4):793–802, 2005.

[36] A. Almqvist and J. Dasht. The homogenization process of the reynolds equation describing compressible flow. To appear in Tribology International.

[37] F. Sahlin, A. Almqvist, S. B. Glavatskih, and R. Larsson. A cavitation algorithm for arbitrary lubricant compressibility. In *World Tribology Congress III*, Washington, D.C., USA, Sep 2005.